Size effects and failure regimes in notched micro-cantilever beam fracture

Devashish Rajpoot [a b], Parag Tandaiya [a], R. Lakshmi Narayan [c], Upadrasta Ramamurty [b d]

[a] Department of Mechanical Engineering, Indian Institute of Technology Bombay, Powai, Mumbai 400076, India

[b] Department of Mechanical and Aerospace Engineering, Nanyang Technological University, Singapore 637331, Republic of Singapore

[c] Department of Materials Science and Engineering, Indian Institute of Technology Delhi, Hauz Khas, New Delhi 110016, India

[d] Institute of Materials Research and Engineering, Agency for Science, Technology and Research (A ∗Star), Singapore 138634, Republic of Singapore

Abstract

Fracture tests using notched micro-cantilever (MC) specimens are increasingly being used to measure the fracture toughness of materials at the micro-scale. Detailed finite element analyses (FEAs) of loading of self-similar micro- and bulk cantilever beam fracture specimens using isotropic, elastoplastic constitutive models, are conducted to critically examine the validity of the toughness data obtained using MC specimens. From the simulated normalized load versus load point displacement and the corresponding normalized energy release rate versus load curves, the transition of the failure regimes from crack propagation to plastic collapse of the uncracked notch ligament are identified. While the crack propagation regime allows for the estimation of valid fracture toughness of the probed material, the plastic collapse regime does not. The effects of specimen aspect ratios, material hardening, and yield criteria on the master curves and transition point are examined. A method to interpret the failure regimes, assess the validity and size effects in micro-cantilever fracture tests is proposed. An expression is derived for the minimum size requirements of MC fracture specimens in order to get a valid fracture test. The data reported in the literature from fracture tests on bulk metallic glasses, nano-crystalline materials and ultra-fine grained materials are assessed using the proposed methodology. The present work has important implications for specimen design, interpretation of failure regimes, and potential size effects in MC fracture tests.

Graphical abstract

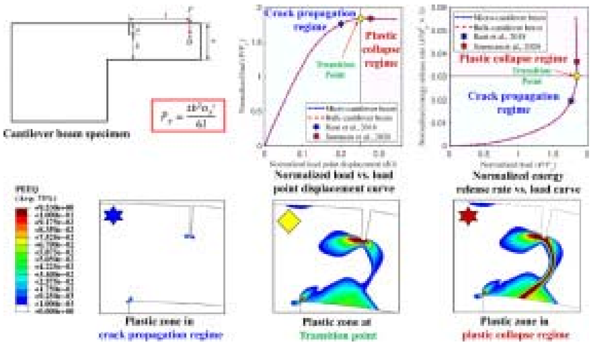

1. Download: Download high-res image (233KB)
2. Download: Download full-size image

Keywords

Micro-cantilever beam fracture tests; Size effect; Fracture mechanics; Finite element analysis; Bulk metallic glasses

1. Introduction

Evaluation of mechanical properties of materials at nanometer to micron scale is an active area of research. This is mainly driven by the following two factors: (a) continued miniaturization of devices, and (b) the desire to connect the micro-scale material properties to the macroscale component performance. The latter aspect is complemented by the substantial advances in the computational tools and power over the past two-three decades. Property characterization of 'small volume' materials is facilitated by the advent of techniques such as nanoindentation and micro-pillar compression [1], [2], [3], [4], [5], [6], [7]. Through these, the size effects in several different materials, i.e., their mechanical properties at the small (micro/nano) scale, were investigated. It was often reported that the properties at the small length scales are substantially different from those at the bulk (mm or larger) scale [8,9]. Recently, the 'micro-cantilever fracture (MCF) test' [5] was extensively used for evaluating the mode I fracture toughness, K_{Ic}, at the microscale. In it, a micro-scale cantilever beam (MCB) of rectangular cross-section containing a small pre-crack near the fixed end is fabricated by focused ion beam (FIB) milling. Then, a nanoindenter with a sphero-conical tip is used to load the free end of the cantilever quasi-statically until the beam fractures. The load (P) versus load-point-displacement (δ) history is recorded and the peak failure load (P_{max}) sustained by the specimen is used to estimate K_{Ic} of the material at the micro-scale.

Recently, Sorensen et al. [9] used MCF tests and reported K_{Ic} of Vitreloy 105 bulk metallic glass (BMG) at the microscale to be ~9.03 MPam, which is an order-of-magnitude smaller than the value of ~95.22 MPam reported by Raut et al. [8] for the same BMG in bulk. Sorensen et al. [9] termed K_{Ic} they measured as the 'intrinsic toughness' of the material and attributed its significantly small value to the size effect. However, a detailed mechanistic rationale for such a size effect was not provided. It is worth noting here that the size effects in Zr-based BMGs are only reported at the *nanoscale* [3,[10], [11], [12], [13], [14], [15]] —that too only for strength and plasticity—and *not at the microscale*. Observation of significant blunting of the notch tip and the spread of plastic zone all the way to the outer boundary of the specimen (see Fig. 6 of Sorensen et al. [9] paper) suggests that the specimen potentially failed due to plastic collapse of the uncracked ligament. This raises questions about the validity of K_{Ic} estimated from the MCF tests because fracture due to crack propagation might not have occured. Such a possibility of failure of MCF specimens through plasticization of the entire uncracked ligament also exists for other ductile and quasi-brittle materials. (Aside, it is worth noting that the confirmation of the mode of failure of a MCF specimen in actual tests is not always possible due to the difficulty in conducting direct *in situ* observations of the deformation, crack initiation, and growth to eventual failure.).

The following larger scientific issue, which encompasses the utility of fracture mechanics (FM), is at stake in using MCF specimens for evaluating K_{Ic}. The success of FM in design of engineering components with assured structural integrity lies in the principal concept of *similitude*. It states that the the stress, strain, and displacement fields ahead of a crack tip are uniquely described by the stress intensity factor, i.e., the fields would be independent of the applied load, crack length, and specimen geometry. This allows for using K_{Ic} measured on a coupon in the laboratory to be utilized for much larger structures (for example). For similitude to hold, either K- or J-dominance conditions (for linear elastic and elasto-plastic FM, respectively) must be satisfied. If not, the measured K_{Ic} or J_c values would not truly represent the intrinsic fracture resistances of the probed material and hence can not be used in engineering design. Does K_{Ic} (or J_c) estimated using MCF specimens meet such conditions for different kinds of elasto-plastic materials is a question that has not been looked into critically yet. In the light of the above, detailed finite element (FE) analyses of notched micro- and bulk-cantilever beam specimens (made of BMGs as well as nanocrystalline (NC) and ultra-fine grained (UFG) alloys) is performed. We considered the two possible regimes of failure that a MCF test specimen could experience and on that basis suggest as to how to mechanistically interpret the validity of the test results. On that basis, some guidelines that researchers can follow for design of specimens for a valid MCF test are proposed.

2. Constitutive models and analysis aspects

The following three different material models are considered in this study: (1) an elastic-perfectly plastic material that yields according to the von Mises [16] (VM) yield criterion (YC), (2) a work hardening solid that yields according to VM YC and strain hardens according to the Ramberg-Osgood hardening [17] (ROH) relationship, and (3) a material that obeys the Mohr-Coulomb (MC) based Anand and Su [18] elastic-viscoplastic deformation model. These are briefly described below. In all the cases, the materials are isotropic because BMGs, NC and UFG materials considered in this study are isotropic, both at the micro- and macro-length scales.

The VM YC is given by the following relationship [16]:

(1) $$f(\sigma_{ij}) = \sqrt{\frac{1}{2}[(\sigma_{11}-\sigma_{22})^2+(\sigma_{22}-\sigma_{33})^2+(\sigma_{33}-\sigma_{11})^2+6(\sigma_{12}^2+\sigma_{23}^2+\sigma_{13}^2)]} = \sigma_y$$

where, σ_{ij} is the Cauchy stress tensor and σ_y is the yield strength. For the cases in which the solid work hardens, the nonlinear hardening response given by the ROH model (Walter and Osgood) [17] is used for capturing the plastic flow behavior:

(2) $$\bar{\varepsilon} = \frac{\bar{\sigma}}{E} + \alpha\frac{\bar{\sigma}}{E}\left(\frac{\bar{\sigma}}{\sigma_{y0}}\right)^{n-1}$$

where, $\bar{\varepsilon}$ is the total effective strain, $\bar{\sigma}$ the VM effective stress, E is the Young's modulus, σ_{yo} is the initial yield strength, α is a coefficient given by $\alpha=0.002\times(E/\sigma_{yo})$,and n is the strain hardening exponent. Note that larger the value of n, smaller is the degree of strain hardening (as $n \to \infty$, the model tends towards elastic-perfectly plastic response). In the present study, E and the Poisson's ratio, ν, are assumed to be 85.6 GPa, and 0.38, respectively [9], while the yield strength in tension, σ_{yt}, is assumed to be 1.87 GPa [8]. Various values of n (= 5, 10, and 20) are considered to explore the effect of different degrees of strain hardening.

Unlike crystalline metals and alloys, BMGs exhibit pressure-sensitive or normal-stress sensitive yield behavior [1,[19], [20], [21]]. Although the degree of pressure sensitivity in them is small, as compared to some other materials such as amorphous polymers, soil and clay, BMGs are found to obey the MC YC [1,[20], [21], [22], [23]]. On that basis, Anand and Su [18] proposed a MC based finite deformation constitutive model, which is applicable for elastic-viscoplastic, pressure-sensitive, and plastically dilatant isotropic amorphous materials undergoing finite deformations. In it, yielding due to shearing occurs at $\theta=\pm(45+\phi/2)$o from the principal directions of stress, where ϕ is the angle of internal friction. $\phi = 0°$ corresponds to the Tresca YC. The Anand and Su [18] constitutive model was reformulated and implemented in an implicit numerical integration procedure by Tandaiya et al. [24] by writing a user material subroutine (UMAT) in ABAQUS/Standard FE program (see Refs. [8,18,[24], [25], [26], [27], [28], [29], [30]] for further details on this model and its implementation). Important material parameters in this model are β(>0) that defines the plastically dilatant behavior, cohesion (c), the MC friction parameter (μ), and the strain rate sensitivity parameter (m). As $m \to 0$, the response becomes rate-independent. This model has been shown to be successful in capturing the response of BMGs under a variety of loading conditions such as tension, compression, bending, indentation, and fracture [8,18,24,25,[28], [29], [30], [31], [32]].

For the simulations using the Anand and Su [18] model in the present study, Vitreloy 105 BMG's material parameters, listed in Table S1 of the Supplementary Information (SI), are used [8,9]. They were chosen to ensure that the simulated σ_y^t and the yield strength in uniaxial compression, σ_y^c, agree with the experimental data. The material parameter *c* is defined as the yield strength in pure shear, and its initial value, c_o, is taken as 980 MPa. Significant strain softening is not observed for Vitreloy 105, hence, *b* is taken as 0, which results in $c_o = c_{cv} = 980$ MPa [8]. A very small value of $m = 0.02$ is chosen to ensure an almost rate-independent response because BMGs tend to be rate-insensitive at room temperature [2,18]. It is expected that the rate of dilatation in tension is higher than that in compression. Hence, as in Anand and Su [18], g_o(T) in tension is taken higher than that in compression, g_o(C), and their values are 0.4 and 0.04, respectively. Various values of $\mu = 0$, 0.008, and 0.05 are considered, based on experiments reported in literature [29,[33], [34], [35], [36]]. A non-zero value of μ leads to tension-compression asymmetry in the yield strength of BMGs while $\mu = 0$ leads to the Tresca YC.

Two-dimensional (2D) plane strain FE analyses (FEAs) of self-similar notched cantilever beam (CB) specimens, schematic drawing of which is displayed in Fig. S1 of SI, are performed. Both micro- and bulk- CB specimens were considered for the simulations. The former's dimensions (load arm length, $l = 11.5$ μm, width, $w = 7.5$ μm, thickness, $t = 6$ μm, crack length, $a = 2.25$ μm, uncracked ligament length, $b = 5.25$ μm, and notch root diameter, $d = 60$ nm) are the same as the ones used in the experiments of Sorensen et al. [9] and are similar to those used by many researchers in their experiments [9,[37], [38], [39], [40]]. A thousand-fold scaled up version ($l = 11.5$ mm, $w = 7.5$ mm, $t = 6$ mm, $a = 2.25$ mm, $b = 5.25$ mm, and $d = 60$ μm) is simulated to represent the bulk CB specimen. Furthermore, simulations on the MCB specimens with various aspect ratios ($t/w = 0.8$, 1.2, 1.6, $l/w = 1.5$, 2.3, 3.1, and $a/w = 0.2$, 0.3, 0.5) are performed to investigate the effect of geometric parameters on the mechanical response of the specimens.

The FE mesh used in the simulations and the magnified view in the region close to the notch tip are displayed in Fig. S2 of SI. The specimen geometry is discretized using continuum 2D plane strain finite elements, labeled CPE4H and available in ABAQUS. This hybrid element is used to alleviate the mesh locking effects due to plastic incompressibility. The mesh consists of a total of 42,318 elements with 32 elements provided along the semi-circumference of the notch root. A fine mesh is employed in the region close to the notch tip so as to accurately capture the stress gradients and shear bands in it. A mesh convergence study has been performed, and accordingly the size of the elements is decided such that the results obtained are mesh insensitive.

Nodes on the specimen's left and bottom surfaces (see Fig. S2 of SI) are constrained in all the degrees of freedom to represent the fixed boundary conditions of the bulk material from which the MCB specimens are machined in the experiments. Downward displacements of 4 μm and 4 mm at the rates of 20 nms−1 and 20 μm s^{-1} are applied at a distance *l* from the notch plane towards the free end in the micro- and bulk-CB specimens, respectively, such that quasi-static loading conditions are maintained. The energy release rate for nonlinear elastoplastic materials, *J*, is calculated using the domain integral formulation available in ABAQUS. A sufficiently large domain that envelops the plastic zone surrounding the notch tip completely is employed for this purpose.

3. Results

3.1. Normalization scheme

The P versus δ and J versus P responses of micro- and bulk- CB specimens (a/w = 0.3) made up of elastic-perfectly plastic material are displayed in Fig. S3 of SI. In both cases, P increases linearly with δ, for up to ~4.66×10−3 N and ~4.66×103 N, respectively. Corresponding values of maximum radius of the crack tip plastic zone, r_p, at maximum P within the linear regime, Pmaxlinear, are ~0.256μm and ~0.256mm, respectively. Note that t, w, and l of the specimens are ≥ 20r_p in both the cases at this juncture. On further loading, the size of the plastic zone becomes substantial, and the P-δ responses becomes nonlinear. The slopes of the P-δ curves eventually become 0 at ~8.26×10−3 N and ~8.26×103 N for micro- and bulk CB specimens, respectively. This corresponds to plastification of the whole uncracked ligament (which will be discussed later).

Under the small scale yielding (SSY) conditions, the quadratic dependence of J on P results in nonlinearity in the J-P response (see Fig. S3(c) and S3(d) of SI). J within the linear regime of the P-δ curve increases slowly first. Following large scale yielding, J increases abruptly and leads to an infinite slope in the J-P curve, due to the plastification of the whole uncracked ligament. Since the CB specimens subjected to fracture under the mode I configuration experience bending, the following dimensionless normalized parameters, which are based on the Euler-Bernoulli beam theory [41], are used in order to bring the responses of micro- and bulk- CB specimens on to a common ground: load $\bar{P}=P/P_y$, J-integral $\bar{J}=J/(\sigma_y^t \times l)$, and load point displacement $\bar{\delta}=\delta/l$. $P_y=(t\times b^2\times \sigma_y^t)/(6\times l)$. Physically, P_y is the load required to cause yielding in a defect free CB having width b and the same t and l as the notched CB, while δ/l signifies the rotation angle of the beam. Plots of $\bar{P}$ versus $\bar{\delta}$ and $\bar{J}$ versus $\bar{P}$ for micro- and bulk CB specimens are displayed in Fig. 1. Complete overlap of the normalized responses of micro- and bulk-CB specimens is noted, which validates the normalization scheme employed here.

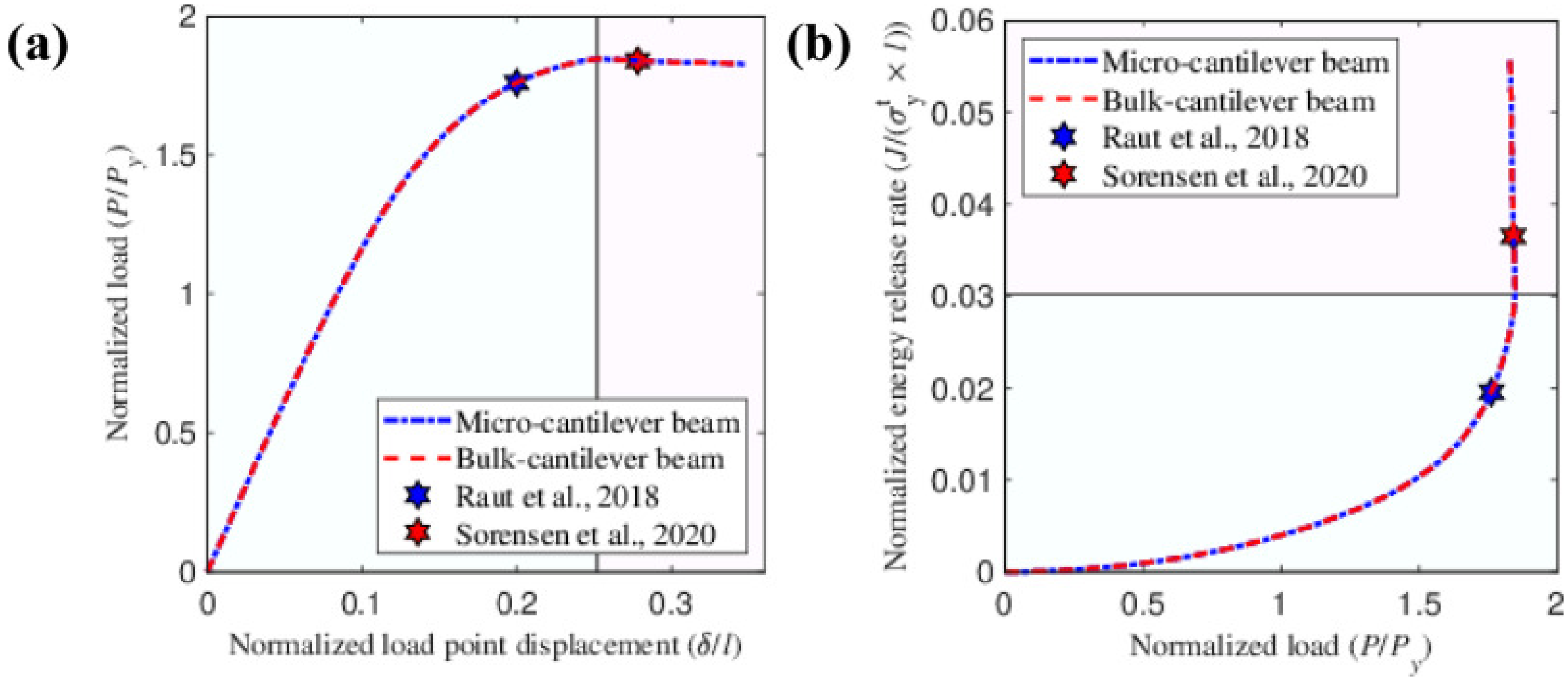

1. Download: Download high-res image (467KB)
2. Download: Download full-size image

Fig. 1. Normalized (a) P versus δ and (b) J versus P curves of micro- and bulk-CB specimens (a/w = 0.3) made of elastic-perfectly plastic material. The vertical line in (a) and the horizontal line in (b) dilineate the transition in the failure regime from fracture to plastic collapse.

To calculate the effective l of other types of notched bend specimens used in experiments that are reported in literature (such as three-point and four-point bend specimens), the moments at their notch planes are divided by P, such that their results can be compared with those of the notched MCB specimens. This methodology enables us to convert the experimental data obtained on other types of bend specimens and reported in literature to an equivalent CB specimen.

3.2. Failure mechanisms/regimes in MCF tests

The $\bar{P}-\bar{\delta}$ and $\bar{J}-\bar{P}$ responses of the CB specimens can be portioned into two distinct regions using horizontal and vertical lines, respectively, as illustrated in Fig. 1. They both correspond to the onset of plastic hinge formation in the uncracked ligament of the notched cantilever specimens. The region to the left of the vertical line in the $\bar{P}-\bar{\delta}$ curve in Fig. 1(a) (or that below the horizontal line in the $\bar{J}-\bar{P}$ curve in Fig. 1(b)) corresponds to the failure mechanism involving fracture by crack propagation, which is desired in the context of testing for fracture. The region to the right of the vertical line (or above the horizontal line) corresponds to failure by plastic hinge formation followed by plastic collapse of the specimen, which is not ideal from the fracture toughness testing perspective as the crack does not propagate.

Experimental J values corresponding to the failure of micro- and bulk-CB BMG specimens taken from literature [8,9] are marked on the $\bar{J}-\bar{P}$ curve displayed in Fig. 1(b). The corresponding $\bar{P}$ values are used to mark the failure points on the $\bar{P}-\bar{\delta}$ curve in Fig. 1(a). Red and blue stars in the normalized $\bar{P}-\bar{\delta}$ and $\bar{J}-\bar{P}$ curves show the failure points of the micro- [9] and bulk- [8] CB specimens, respectively. They lie to the left and right sides of the line delineating the fracture regime in the $\bar{P}-\bar{\delta}$ curve, respectively.

Contour plot of equivalent plastic strain (PEEQ) obtained from the elastic–perfectly plastic FE simulation of the CB specimen corresponding to $a/w = 0.3$ at failure point of the bulk specimen (blue star symbol in Fig. 1), at the onset of plastic hinge formation (vertical line), and at failure point of the MCB specimen (red star symbol in Fig. 1) are displayed in Fig. 2 (a), (b), and (c), respectively. Initially, in both the CB specimens, plastic deformation occurs around the notch tip and at the bottom of the specimens. At the point of failure, the plastic zone size ($r_p \le (1/25) \times (a,w,l)$) in the bulk CB specimen remains small (see Fig. 2(a)). In contrast, the plastic zones grow and link up upon further loading in the MCB specimen (see Fig. 2(b)). The eventual failure of the MCB specimen occurs because of plastification of the whole uncracked ligament leading to plastic collapse.

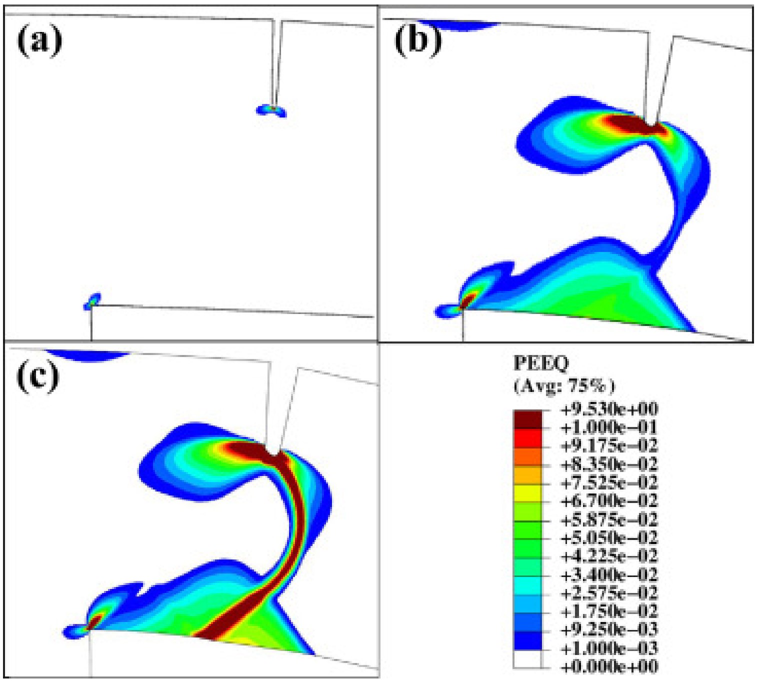

1. Download: Download high-res image (341KB)
2. Download: Download full-size image

Fig. 2. Contour plots of equivalent plastic strain (PEEQ) (a) at failure point of the bulk specimen (corresponding to Raut et al. [8], blue star in Fig. 1), (b) at failure regime transition point marked by the vertical line in Fig. 1a, and (c) at failure point of the MCB

specimen (corresponding to Sorensen et al. [9], red star in Fig. 1) corresponding to plastic collapse.

3.3. Effect of geometric parameters on the $\bar{P}-\bar{\delta}$ and $\bar{J}-\bar{P}$ curves

The effect of various geometric parameters such as *t/w, a/w*, and *l/w*, which define the aspect ratio of the MCB specimens, on the mode I fracture response of the CB specimens made up of an elastic-perfectly plastic material is investigated next. For this, *t/w* values of 0.8, 1.2, and 1.6 were considered, where *t* is changed according to the required *t/w* ratio while keeping other geometrical parameters constant. The $\bar{P}-\bar{\delta}$ and $\bar{J}-\bar{P}$ curves for various *t/w* are displayed in Fig. S4(a) and (d) of SI, respectively. For all the specimens, the simulated responses coincide, and are exactly like those displayed in Fig. 1 (a) and (b).This is because P_y, which is used to normalize *P*, contains *t*. Recall that *J* is defined as the energy released per unit increase in fracture surface area (Δa×t) [42]. Thus, the effect of *t* on *J* is also eliminated, which results in overlapping $\bar{J}-\bar{P}$ curves. Yellow star symbols in Fig. S4 of SI correspond to the onset of plastic hinge formation. Contour plots of PEEQ at the failure ($\bar{\delta}$ = 0.35) of MCB specimens corresponding to *t/w* = 0.8, 1.2, and 1.6 are displayed in Fig. S5(a), (b), and (c) of SI, respectively. It can be noted that *t* does not affect the contour plots of PEEQ at the same normalized $\bar{\delta}$.

Next, FEAs of MCB specimens having various crack length to width ratios, *a/w* = 0.2, 0.3, and 0.5 are carried out. In these simulations, the specimen's crack length *a* is varied such that the desired *a/w* is obtained and the other dimensions are kept the same as in the reference specimen. Resultant $\bar{P}-\bar{\delta}$ and $\bar{J}-\bar{P}$ curves corresponding to *a/w* = 0.2, 0.3, and 0.5 are displayed in Fig. S4(b) and (e) of SI, respectively. These plots broadly resemble those presented in Fig. 1. A notable observation is that the slope of the $\bar{P}-\bar{\delta}$ curve in the linear regime increases with an increase in *a/w*. Thus, it appears that the stiffness of the specimen increases with the *a/w* ratio. This trend appears to be counter-intuitive *prima facie*. However, the dependence of the normalization load, P_y to the square of the uncracked ligament length (b^2) can be used to explain it. An increase in *a*, at a fixed *w*, decreases *b* and leads to a decrease in P_y, which in turn leads to an increase in $\bar{P}$ for the same $\bar{\delta}$.On further loading, the $\bar{P}-\bar{\delta}$ curve deviates from linearity due to significant plastic deformation (where 20rp≥t,w,l). Thus, different *a/w* ratios result in a family of $\bar{P}-\bar{\delta}$ and $\bar{J}-\bar{P}$ curves. Star symbols on these curves represent the points corresponding to onset of plastic hinge formation. It occurs at $\bar{\delta}$ = 0.25 and 0.19 for *a/w* = 0.3 and 0.5, respectively, while the corresponding $\bar{P}$ is the same. Plastic hinge formation is not observed for *a/w* = 0.2 specimen, which is discussed later. The slope of the $\bar{P}-\bar{\delta}$ curve for *a/w* = 0.3 specimen becomes 0 immediately after the plastic hinge formation. After the plastic hinge formation in *a/w* = 0.3 specimen, slope of the $\bar{J}-\bar{P}$ curve becomes infinity. However, the same is observed in *a/w* = 0.5 specimen after a significant drop in $\bar{P}$. Overall, $\bar{J}$ corresponding to plastic hinge formation decreases with increase in *a/w*.

Contour plots of PEEQ for *a/w* = 0.2, 0.3, and 0.5 are displayed in Fig. S5 (d), (e), and (f) of SI, respectively. Initially plastic deformation is observed around the notch root and at the bottom of the beam. On further loading, both the regions undergoing plastic deformation linkup and lead to failure of a/w = 0.3, and 0.5 specimens. Also, in these two cases, it is observed that the plastic deformation localizes in the uncracked ligament with increase in a/w. However, linking of regions undergoing the plastic deformation is not observed in the a/w = 0.2 specimen. In this particular case, it is noted that the left lobe of the plastic zone near the notch tip links up with the plastic zone emanating from the tensile side of the root of the CB specimen while the uncracked ligament does not become fully plastic.

It is observed in our simulations that $\bar{\delta}$ corresponding to plastic hinge formation decreases with increasing a/w. Thus, beams having smaller b, or those having higher a/w, plastify sooner than those with bigger b because the size of the region that needs to undergo plastic deformation for full plastification of the ligament is smaller in the former.

The $\bar{P}-\bar{\delta}$ and $\bar{J}-\bar{P}$ curves of MCB specimens corresponding to l/w = 1.5, 2.3, and 3.1 are displayed in Fig. S4(c), and (f) of SI, respectively. The $\bar{P}-\bar{\delta}$ curves for l/w = 2.3, and 3.1 almost overlap within the elastic regime. On further loading they deviate from linearity due to significant plastic deformation and lead to plastic hinge formation (indicated by the star symbols on the plots) which eventually cause the failure of the specimens. Thus, different l/w ratios result in a family of $\bar{P}-\bar{\delta}$ and $\bar{J}-\bar{P}$ curves. However, plastic hinge formation for all MCB specimens occurs at a similar $\bar{\delta}$ of 0.23 and $\bar{J}$ of 0.03, irrespective of the l/w.

Contour plots of PEEQ for l/w = 1.5, 2.3, and 3.1 are displayed in Fig. S5(g), (h), and (i) of SI, respectively. Similar to other MCB specimens, region near the notch root and the bottom of the beam undergo plastic deformation. The right lobe of the plastic zone near the notch tip links up with the plastic zone at the bottom of the beam to form a plastic hinge and cause the failure of the beam due to plastic collapse. The contour plots of PEEQ in the region undergoing plastic deformation in all the cases are almost similar at the same normalized load point displacement δ/l = 0.35 (see Fig. S5(g), (h), and (i) of SI) corresponding to impending plastic collapse.

The effect of geometric parameters on the responses of MCB specimens can be summarized as follows. The $\bar{P}-\bar{\delta}$ and $\bar{J}-\bar{P}$ curves are independent of the thickness of the specimen. Effect of l/w on specimen responses is not significantly different for specimens with $l/w \geq 2.3$. Different a/w and l/w ratios result in a family of $\bar{P}-\bar{\delta}$ and $\bar{J}-\bar{P}$ curves.

3.4. Effect of material hardening on the $\bar{P}-\bar{\delta}$ and $\bar{J}-\bar{P}$ curves

The effect of strain hardening exponent, n, on the mechanical response of the MCF specimens made up of a material obeying ROH relationship is investigated next. While Fig. 3(a) shows the true stress-strain (σ-ε) responses of the material with different values of n, the $\bar{P}-\bar{\delta}$ and $\bar{J}-\bar{P}$ responses of the MCB specimens are displayed in Fig. 3(b) and (c), respectively. In all the $\bar{P}-\bar{\delta}$ curves, nonlinearity starts at $\bar{\delta}$ = 0.1, once significant plastic deformation sets in. While the slope of the $\bar{P}-\bar{\delta}$ response of the elastic-perfectly plastic material becomes 0 when the whole ligament plastifies, those for ROH materials harden; the extent of hardening depends on n. Star symbols on the curves indicate the onset of plastic hinge formation. As seen, the corresponding $\bar{\delta}$ and $\bar{P}$ increase with a decrease in n. The $\bar{J}$ - $\bar{P}$ curves, which are identical within the linear regime of $\bar{P}-\bar{\delta}$ curve, diverge within the plastic regime with the slope of the $\bar{J}-\bar{P}$ curves decreasing with increasing degree of strain hardening (decreasing n). But, $\bar{J}$ corresponding to the onset of plastic hinge formation increases with increasing degree of strain hardening. This implies that if the specimen fails due to plastic hinge formation leading to plastic collapse, it can withstand higher load, provided the material undergoes greater degree of strain hardening.

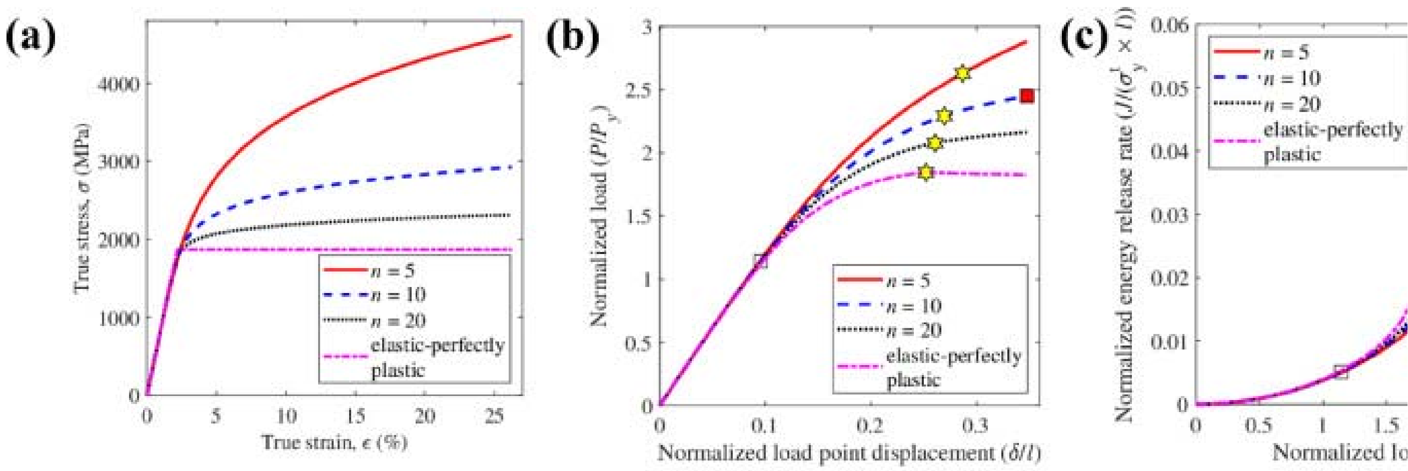

1. Download: Download high-res image (420KB)
2. Download: Download full-size image

Fig. 3. (a) True stress versus true strain (σ-ε), (b) $\bar{P}-\bar{\delta}$, and (c) $\bar{J}-\bar{P}$ curves for various values of ROH exponent, n. Star symbols indicate the transition in failure regime from fracture to plastic collapse.

Contour plots of PEEQ on specimens in deformed configuration for n = 5, 10, 20, and elastic-perfectly plastic materials at $\bar{\delta}$ = 0.35 are displayed in Fig. 4. In all cases, the plastic zones develop ahead of the notch tip and the bottom of the CB specimen as discussed earlier. However, there are subtle differences in the plastic zones of specimens made up of materials undergoing different degrees of strain hardening. It is interesting to observe from Fig. 4(a)–(c) that for materials that undergo hardening (n = 5, 10, and 20), the top surface of the CB near its root under tension also undergoes plastic deformation and links up with the left lobe of the plastic zone near the notch root. The same is not observed for the elastic-perfectly plastic material. Alternately, the intensity of plastic strain in the plastic zones increases with decrease in the degree of hardening, which is along expected lines (see Fig. 4). Thus, the plastic strain is most localized in the specimen made up of the elastic-perfectly plastic material.

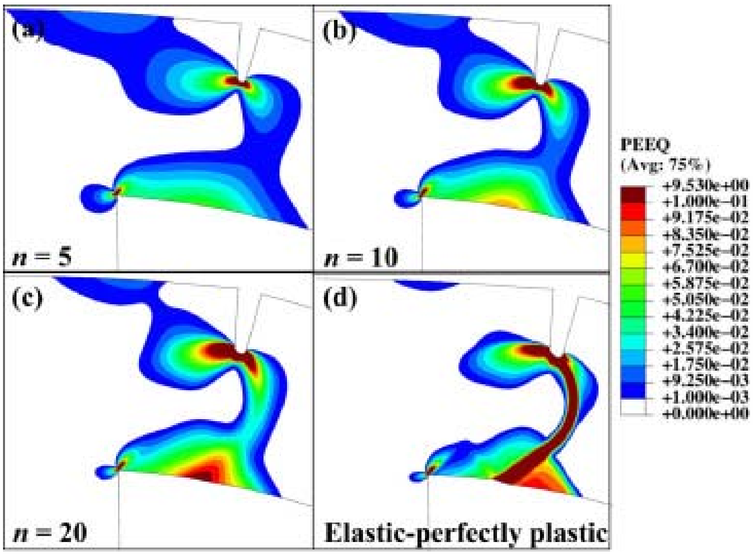

1. Download: Download high-res image (365KB)
2. Download: Download full-size image

Fig. 4. Contour plots of PEEQ at impending plastic collapse ($\bar{\delta}$ = 0.35) for specimens made up of (a) n = 5, (b) n = 10, (c) n = 20, and (d) elastic–perfectly plastic materials.

3.5. Effect of YC and material model on the $\bar{P}$–$\bar{\delta}$ and $\bar{J}$–$\bar{P}$ responses

In the preceding sections, we examined the response of MCB specimens made up of materials obeying the VM YC, exhibiting elastic-perfectly plastic response and strain hardening following the ROH equation. In this sub-section, we investigate the effect of choice of Tresca and MC YC on the response of MCF specimens. While the Tresca and VM YC are suitable for ductile, isotropic, polycrystalline elastoplastic materials such as nano-crystalline and ultrafine grained materials, MC YC is suitable for isotropic, pressure sensitive materials such as metallic glasses.

Tensile stress-strain (σ-ε) responses of BMGs using the Anand and Su [18] constitutive model corresponding to μ = 0, 0.008, and 0.05 are displayed in Fig. 5(a). Here μ = 0 corresponds to the Tresca YC. All the σ-ε responses overlap within the linear regime because the same values of E and ν is used in all the simulations. Different σ^t_y are observed due to the use of different values of μ. σ^t_y of the material decreases with an increase in μ because of increased tension-compression asymmetry in strength. Beyond σ^t_y, ε increases for the constant value of σ as the response is assumed as elastic-perfectly plastic. In this work, we considered Vitreloy 105 BMG which does not show strain softening, although most of the amorphous alloys/BMGs are reported to exhibit strain softening [1,8,18,30].

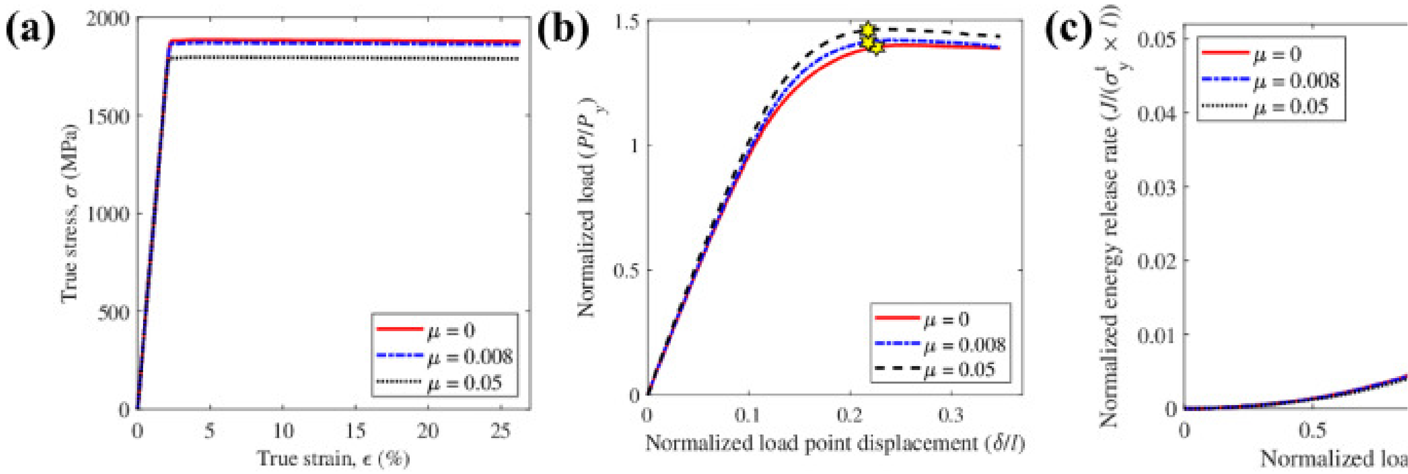

1. Download: Download high-res image (348KB)
2. Download: Download full-size image

Fig. 5. (a) True tensile stress versus strain (σ-ε), (b) $\overline{P}-\overline{\delta}$, and (c) $\overline{J}-\overline{P}$ curves for various values of the MC friction parameter, μ. Star symbols indicate the transition in failure regime from fracture to plastic collapse.

The $\overline{P}-\overline{\delta}$ and $\overline{J}-\overline{P}$ responses of MCF specimens obeying the MC based Anand and Su [18] model are displayed in Fig. 5(b) and (c), respectively. Again, the yellow star symbols on the curves indicate the onset of plastic hinge formation in individual cases. A small increase in the $\overline{P}$ values corresponding to onset of plastic hinge formation with μ is noted. Also, a higher μ results in the BMG sustaining greater load up to failure.

Contour plots of maximum principal logarithmic plastic strain ($\ln\lambda_1^p$) for above cases at $\overline{\delta} = 0.35$ are displayed in Fig. 6. In all cases, link up of the right lobe of the plastic zone near the notch tip with the bottom plastic zone leads to the plastification of the full ligament that results in failure of the sample. Plastic deformation progresses in the form of discrete shear bands. No prominent effect of μ on the deformation morphology could be seen.

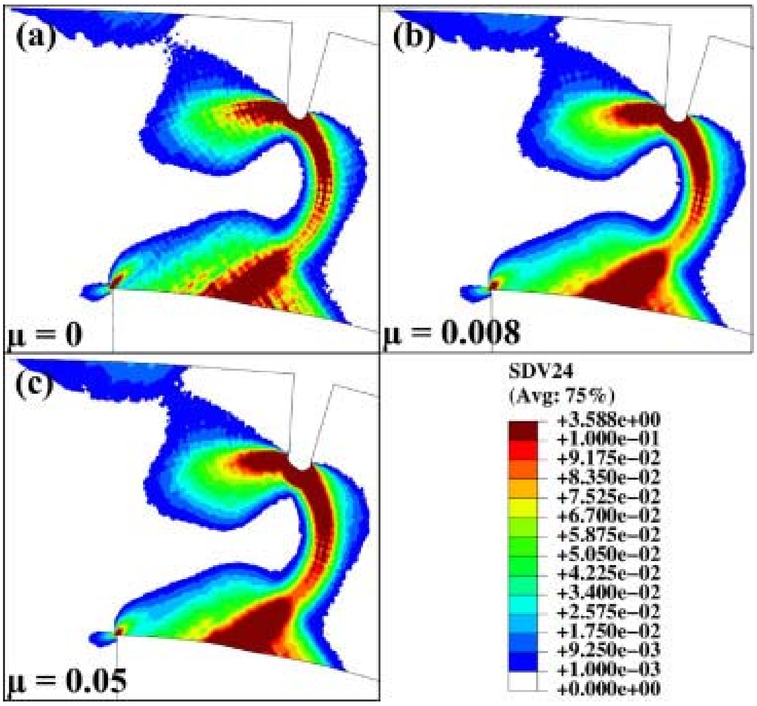

1. Download: Download high-res image (580KB)
2. Download: Download full-size image

Fig. 6. Contour plots of $\ln\lambda_{1p}$ in specimens having (a) $\mu = 0$, (b) $\mu = 0.008$, and (c) $\mu = 0.05$ at $\bar{\delta} = 0.35$.

4. Discussion

4.1. Validity of the MCF tests

A MCF test could be invalid if it did not lead to crack propagation in the specimen. Therefore, and with reference to the $\bar{P}-\bar{\delta}$ curve in Fig. 1(a), a MCF test would be valid if and only if the point at which the specimen fails lies to the left of the transition point (which is indicated by a vertical line in Fig. 1(a), and yellow star symbols in Figs. S4(a)–(c), 3(b), and 5(b)). In the crack propagation regime, it is observed from the contour plots of PEEQ and $\ln\lambda_{1p}$ that the size of the plastic zone is small and it satisfies the SSY condition, which makes the stress intensity factor, K_I, an appropriate fracture characterizing parameter. Alternatively, large scale yielding (LSY) would be applicable if SSY does not hold and the plastic zone size is large (as in the case of ductile elastoplastic solids). In such a scenario, J should be used as an appropriate fracture characterizing parameter. However, if the entire crack ligament undergoes plastic deformation forming a plastic hinge corresponding to a point beyond the transition point in the $\bar{P}-\bar{\delta}$ curve, even J would not be a suitable fracture characterizing parameter as no J-dominant annulus surrounding the notch tip would exist.

If, in a MCF experiment, fracture happens at an advanced stage of LSY when the ligament has formed a plastic hinge, then, J alone may not be able to characterize the near-tip fields and hence J_c would not be a valid measure of fracture toughness. In such cases, two parameter fracture theories such as J-Q theory [43] may need to be employed to characterize the crack tip fields. However, with extensive plastic deformation, even two-parameter theories may breakdown and three parameter fracture mechanics theories such as J-A_2-A_4 theory [44,45] based on the asymptotic analysis of the crack tip field may be required.

Formation of plastic hinge is followed by plastic collapse of the specimen at which $\frac{d\bar{J}}{d\bar{P}} \to \infty$ as observed in Figs. 1(b), S4(d)–(f), 3(c) and 5(c). Thus, failure by plastic collapse may precede that by crack propagation. If this happens in a MCF specimen, it implies that fracture toughness of the material *can not* be measured with that specimen. In such a scenario, the values of J at which the specimen notionally fails would be lower than the actual fracture toughness J_c. Interpreting such lower J as the fracture toughness of the material being probed will, inevitably, lead to wrong conclusions about the size effects on fracture toughness of the material. It is observed from the available literature that many of the MCF specimens made up of ductile materials fail due to plastic collapse [9,38,46,47]. Such tests cannot be considered as valid fracture tests.

One needs to ensure that they have a valid fracture test as evidenced from the direct observation of crack propagation before plastic collapse can set in. However, direct *in situ* observation of micro-cantilever specimen deformation and failure may be difficult. In the absence of such direct observations, excessive crack blunting and plastic hinge formation in the ligament and its subsequent rotation during the testing of ductile elastoplastic materials, may give an impression of crack propagation if one records only the P-δ response. One also needs to examine the failed MCB specimen to convince themselves of crack propagation in the specimen.

An alternative approach to interpret the MCF test data is as follows. One can plot the $\bar{P}-\bar{\delta}$ and $\bar{J}-\bar{P}$ curves for one's specimen based on FEAs of the MCF specimen and then mark the experimentally observed failure point of the specimen on those curves. If the failure point falls sufficiently to the left of the transition point, one can be assured of genuine fracture or failure by crack propagation. Then, the measured fracture toughness would be valid. And, if the measured fracture toughness is different from that measured from a bulk specimen, one could conclude positively about a possible size effect on fracture toughness. This would warrant an investigation into the change in fracture mechanism between bulk and micro-scale specimens. If, however, the failure point of the specimen happens to fall to the right of the transition point, it is highly likely that the failure of the specimen happened due to plastic collapse and the fracture test may not be valid. In such cases, one should refrain from concluding anything about the size effects or intrinsic fracture toughness of the material. The proposed criterion for validity of MCF tests is applicable not only for non-hardening materials but also for strain hardening and strain softening materials.

4.2. Application of the proposed micro-cantilever failure regimes to BMGs

In the light of the above results, the analysis performed by Sorensen et al. [9] and the interpretation of their experimental results are discussed below. We performed FEAs of loading of the MCB fracture specimen used in the work of Sorensen et al. [9] employing the MC based constitutive model of Anand and Su [18] with μ = 0.008 and geometric and other material parameter values mentioned in Section 2. The resulting normalized $\bar{P}-\bar{\delta}$ and $\bar{J}-\bar{P}$ curves are displayed in Fig. 7. The P-δ curves and J at failure obtained using the simulation agree well with the reported experimental data of Sorensen et al. [9]. The failure point of the MCF specimens in Sorensen et al.'s [9] experiment is marked as filled green star symbol on the $\bar{P}-\bar{\delta}$ and $\bar{J}-\bar{P}$ curves. As can be observed from Fig. 7(a), the failure point falls to the right of the transition point (indicated by the vertical line in Fig. 7(a)). This suggests that the MCB fracture specimens in Sorensen et al.'s [9] experiments failed not due to crack propagation but by plastic collapse. Indeed, extensive notch blunting and plastic hinge formation in the ligament upon plastic collapse can be clearly seen in the SEM images reported by Sorensen et al. [9] (see Fig. 8(a), which is reproduced with permission from Sorensen et al. [9]). Considerable plastic deformation around the notch and bottom of the beam in the form of shear bands, which is identical to what is predicted from the present FE simulations (see Fig. 6(b)), can be seen.

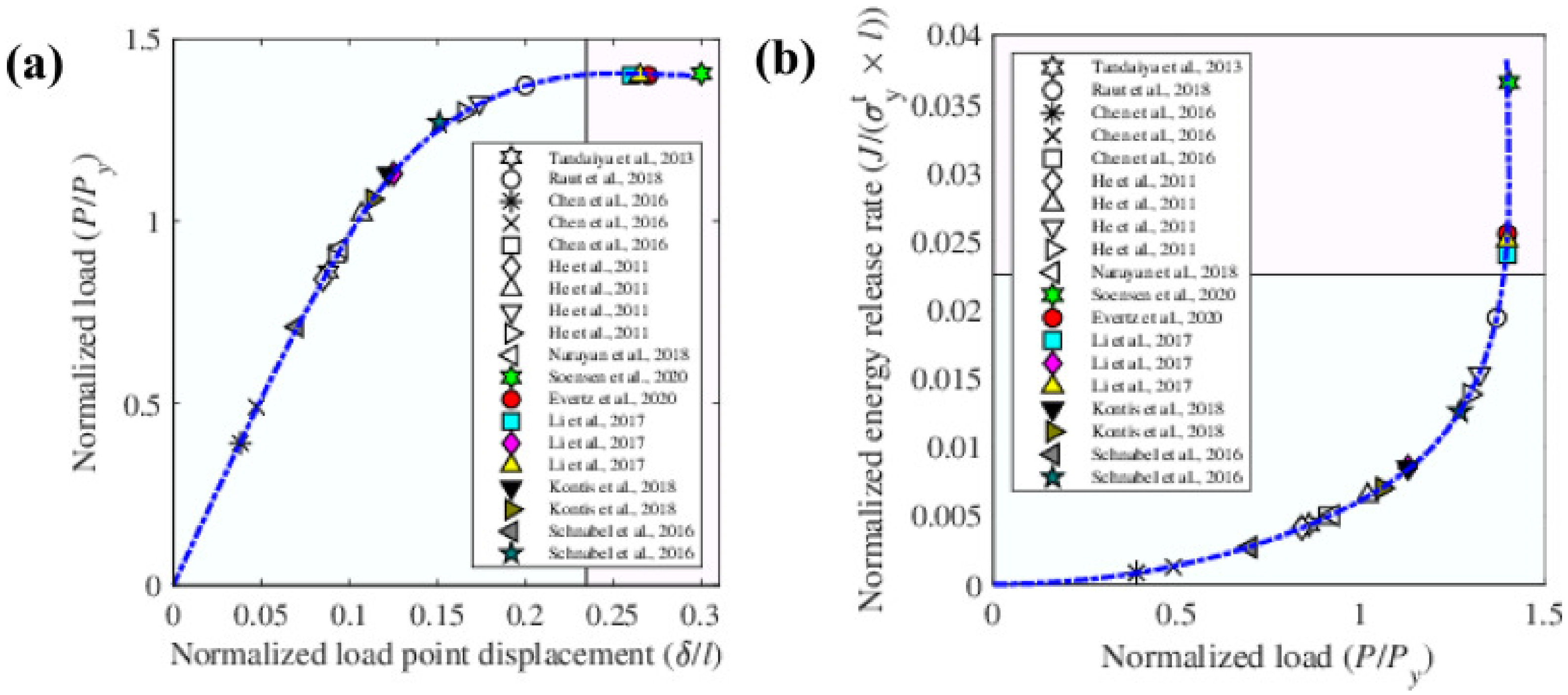

1. Download: Download high-res image (589KB)
2. Download: Download full-size image

Fig. 7. Failure points of micro and bulk specimens marked on (a) $\bar{P}-\bar{\delta}$ and (b) $\bar{J}-\bar{P}$ curves of CB specimens made of BMGs. The master curves are obtained from FE simulations using the MC based Anand and Su [18] model. The filled symbols correspond to the failure points of MCB specimens and other symbols correspond to the failure of bulk specimens.

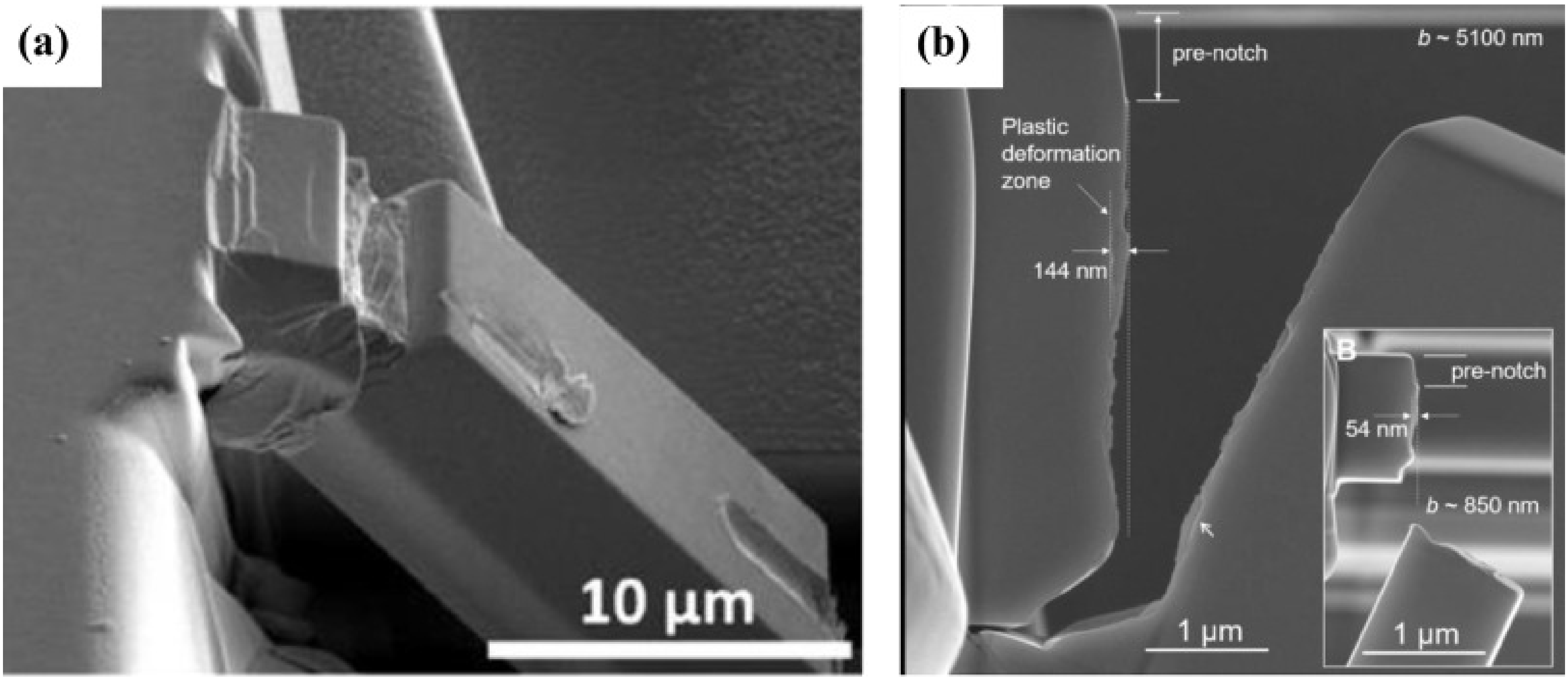

1. Download: Download high-res image (505KB)
2. Download: Download full-size image

Fig. 8. SEM images of the BMG specimens lying in the (a) failure due to plastic collapse regime [9], and (b) fracture due to crack propagation regime [48]. Reproduced with permission [65,66] from [9,48].

For their FEAs, Sorensen et al. [9] used VM YC and assumed exceptional hardening in Vitreloy 105 BMG with σyt increasing from initial value of 1950 to 3250 MPa at 0.005 plastic strain. This was done, presumably, to obtain a match between the simulated and experimental *P*-δ curves. In doing so, they ignored the well established fact that most monolithic BMGs are pressure or normal stress sensitive and follow the MC YC [1,20,49,50]. More importantly, they do not undergo strain hardening but rather exhibit elastic-perfectly plastic or strain-softening behaviour [1,8,18]. Such deviations from the actual constitutive responses cannot be rationalized by recourse to size effects, since such effects are observed only at nm length scales [3,[10], [11], [12], [13], [14], [15]]. However, size effects are not expected in the experiments of Sorensen et al. [9], because their specimen dimensions are in the range of a few µm.

A particular reason for the invalidity of the MCF tests in the context of BMGs is the following. Plasticity in BMGs at the micro- and macro-scales manifests through localization of flow. In the absence of a microstructure, unhindered propagagtion of 'shear bands' leads to the failure of the unnotched specimens in uniaxial tension. Upon propagating over a critical length, the shear bands become shear cracks. In the context of a notched specimen, shear band mediated 'ductile' fracture of a BMG is governed by the criterion that the propagating crack will become unstable only after a certain plastic strain is exceeded over a characteristic length scale [30]. The latter is often several tens of microns. Indeed, Tandaiya et al. [30] found that for Vitreloy-1 BMG stable crack growth occurs inside a dominant shear band ahead of the notch tip upto a characteristic length scale of ~60 μm, beyond which crack propagates catastrophically. Furthermore, based on their FEAs and experiments, Tandaiya et al. [29] found that the fracture initiation in Vitreloy-1 BMG was very well predicted by attainment of a critical plastic strain of 0.1 over a critical distance of ~60 μm from the notch tip. For the Vitreloy 105 BMG examined by Sorensen et al. [9], this characteristic length scale is ~80 μm as reported in Ruat et al. [8]. Since the uncracked ligament length in the experiments of Sorensen et al. [9] is smaller than this, the critical condition for shear bands to turn into unstable shear cracks is never attained.

The applicability of the proposed MCF regimes to identify the validity of other fracture tests on BMGs, performed on both microscale as well as bulk specimens, reported in literature is explored next. Failure points taken from literature are mapped on the $\bar{P}-\bar{\delta}$ and $\bar{J}-\bar{P}$ curves displayed in Fig. 7. All the failure points of the bulk specimens [8,30,[51], [52], [53]] lie to the left of the transition point in the regime implying fracture due to crack propagation and hence valid fracture toughness measurements. While the failure points of some MCF specimens [37], [38], [39] lie to the left of the transition point, others (such as that reported by [9,38,46]) lie to the right. A SEM image of the failed MCF specimen taken from Qu et al. [48] is displayed in Fig. 8(b). It can be noticed that the size of the plastic zone surrounding the crack tip is small and the specimen failed due to crack propagation, which indicates that this was a valid fracture test.

4.3. Application to nanocrystalline and ultra fine grained materials

The results reported in the present paper are not restricted to BMGs but can also be applied to other isotropic elastoplastic solids as well. We examine this possibility for nanocrystalline (NC) and ultra-fine grained (UFG) materials. (We do not consider coarse grained metals as the MCF specimens would be single crystalline in such cases. For brittle materials like ceramics and inorganic and non-metallic glasses, the fracture toughness values will be so low that the failure points would always lie to the left of the transition point, i.e., the MCF tests would be valid even when the specimen sizes are micron-scaled.) Failure points of the microscale [54], [55], [56], [57], [58] and bulk [59] NC alloy specimens taken from literature are plotted on the $\bar{P}-\bar{\delta}$ and $\bar{J}-\bar{P}$ master curves of a MCF specimen subjected to mode I loading obtained from FE simulation, as displayed in Fig. 9. For generating these master curves, the material is assumed to be elastic-perfectly plastic and obeys VM YC. (A log-log scale is used keeping the large range of reported values in mind.) As seen, all the failure points lie in the regime involving fracture due to crack propagation. Locations of the failure points suggest that these fracture tests are valid. A representative SEM image of a MCB specimen made up of a NC material (NbMoTaW), tested in mode I loading, and taken from Xiao et al.'s [55] work is displayed in Fig. 10. Negligible plastic deformation around the notch tip confirms the validity of the test performed. This is because NC alloys show limited ductility that results in small plastic zone sizes.

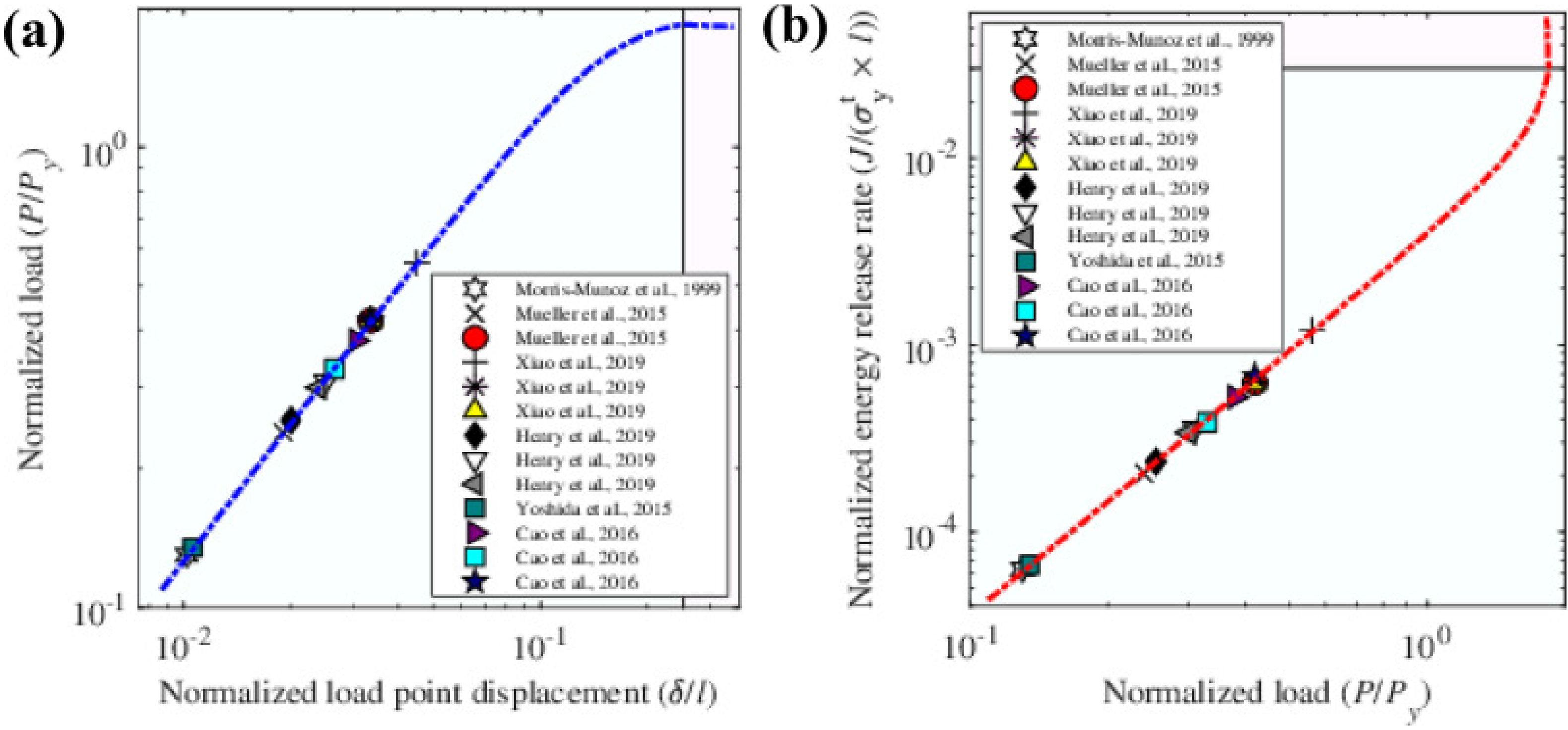

1. Download: Download high-res image (533KB)
2. Download: Download full-size image

Fig. 9. Failure points of microscale and bulk specimens marked on (a) $\bar{P}-\bar{\delta}$ and (b) $\bar{J}-\bar{P}$ curves of a MCB specimen made of nano-crystalline materials. The open symbols correspond to the failure points of bulk specimens and other symbols correspond to the failure of MCB specimens.

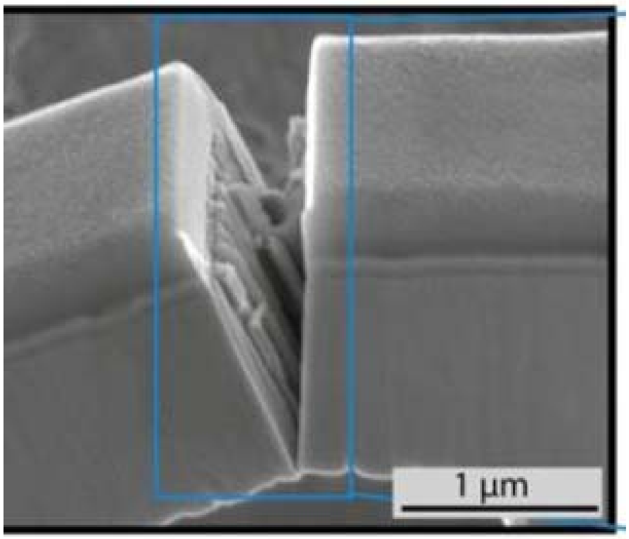

1. Download: Download high-res image (177KB)
2. Download: Download full-size image

Fig. 10. A representative SEM image of a nanocrystalline MCB specimen tested in mode I. Reproduced with permission from [55]. Reproduced with permission [67] from [55].

Reported values of the failure points for the microscale as well as bulk UFG alloy specimens, assumed to be elastic-perfectly plastic and obeying VM YC, subjected to mode I loading conditions are plotted on $\bar{P}-\bar{\delta}$ and $\bar{J}-\bar{P}$ curves in Fig. 11. Failure points of the bulk specimen [60] and some MCB specimens [47,61] lie in the crack propagation regime. However, the result of the MCB fracture tests performed by Issa et al. [47] on ultra-fine grained Chromium falls in the regime of failure due to plastic collapse. Representative SEM images of the failed specimens lying in the regimes of fracture due to crack propagation and failure due to plastic collapse are displayed in Fig. 12(a) and (b), respectively. These SEM images indicate that the former specimen has a smaller plastic zone size while the whole ligament is plastic for the latter specimen and is large enough to interact with the boundaries of the specimen such that the validity of fracture test is questionable.

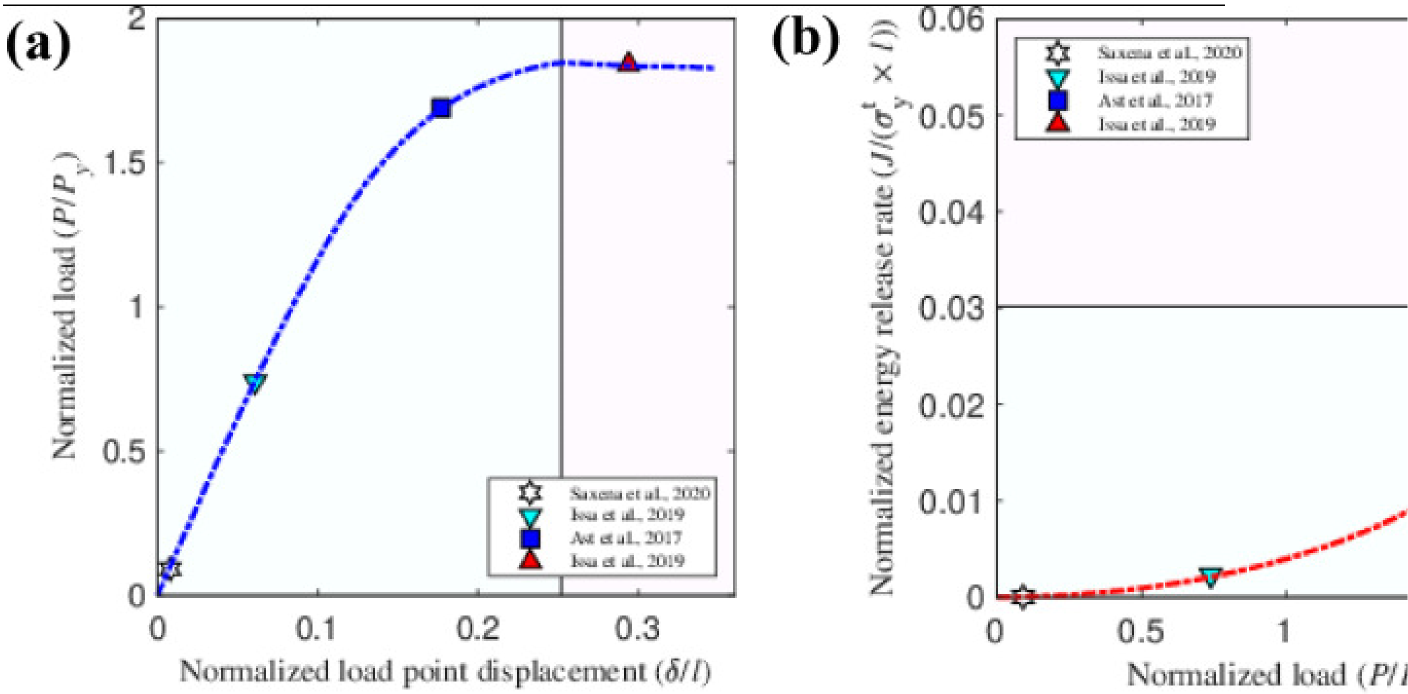

1. Download: Download high-res image (406KB)
2. Download: Download full-size image

Fig. 11. Failure points of micro-scale and bulk specimens marked on (a) $\bar{P}-\bar{\delta}$ and (b) $\bar{J}-\bar{P}$ curves of MCB specimens made of ultra-fine grained materials. The open symbols correspond to the failure points of the bulk specimen and the filled symbols correspond to the failure points of MCB specimens.

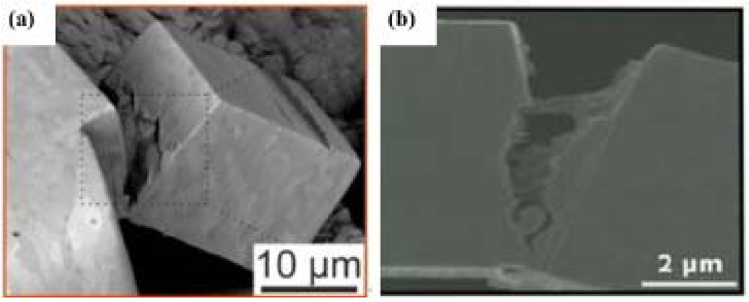

1. Download: Download high-res image (139KB)
2. Download: Download full-size image

Fig. 12. SEM images of the failed ultra-fine grained specimens lying in the (a) fracture due to crack propagation [61], and (b) failure due to plastic collapse regimes [47]. Reproduced with permission [68] from [61].

4.4. Design of MCF specimens for a valid fracture test

The present set of results allow for making recommendations on the desired design (in particular, dimensions) of the MCF specimens in order to ensure valid fracture tests that yield meaningful fracture toughness data. For that, the failure point of the specimen should always be to the left of the transition point on the $\bar{P}-\bar{\delta}$ curve. Let this transition point or the point of onset of plastic hinge formation be denoted by $\bar{P}_{tr}$, whose value can be obtained from a master curve, such as that in Fig. 1(a). Typically, one has an *in situ* small scale testing setup which has a limit on the maximum load it can apply (say P_{max}) and the maximum load-point-displacement it can record (say δ_{max}). One wants to limit the dimensions of the MCF specimen in such a way that during the test, the load sustained by the specimen should not exceed P_{max} and the load-point-displacement should not exceed δ_{max}. Let P_f represent the failure load of the MCF specimen. Using these parameters as the boundary conditions, we will derive an expression for the minimum dimensions that must be employed for a valid MCF test specimen.

To ensure that the specimen failure point is to the left of the transition point, we require:

(3) $$\bar{P}_f < \bar{P}_{tr}/\chi$$

$$\frac{P_f}{P_y} < \bar{P}_{tr}/\chi$$

$$\frac{\chi(6P_f l)}{(tb^2\sigma_y^t)} < \bar{P}_{tr}$$

Let α=aw, β=tw and γ=lw. $\chi > 1$ is a safety factor to ensure that the failure point lies sufficiently to the left of the transition point on the $\bar{P}-\bar{\delta}$ curve. The ligament length b=w−a=(1−α)w. Substituting them in Eq. (3), we get,

(4) $$\frac{6\gamma\chi P_f}{\beta(1-\alpha)^2\sigma_y^t\omega_{min}^2} < \bar{P}_{tr}$$

Simplifying the above inequality, we get the expression for the minimum width, w_{min}, of the MCB fracture specimen as:

(5) $\omega_{min} > \sqrt{\frac{6\gamma\chi P_f}{\beta(1-\alpha)^2\sigma_y^t \bar{P}_{tr}}}$

Thus, it is recommended that MCB fracture specimens should be designed with w sufficiently greater than that given by Eq. (5) in order to have a good chance of getting a valid fracture test.

We will now utilize Eq. (5) to estimate the w_{min} of the MCB specimens that is required for performing a valid mode I fracture test in two studies where the estimated fracture toughness is contentious. Assuming χ = 3 to calculate w_{min} required to perform a valid MCB fracture test. Based on the aspect ratio of MCF specimen used by Sorensen et al. [9], we consider α = 0.3, β = 0.8, and γ = 1.53. The Pf value for Vitreloy 105 in Sorensen et al.'s [9] experiment is ~9.1 mN and σyt can be taken as 1.87 GPa [8]. $\bar{P}_{tr}$ =1.4 from Fig. 7(a). Substituting these numbers in Eq. (5) yields the result that w_{min} of the MCB specimen to get a valid fracture test should be greater than 15.63 μm, whereas it was only 7.5 μm in the experiments of Sorensen et al. [9]. Due to this insufficiency in meeting the required conditions for obtaining a valid fracture test, failure by plastic collapse precedes that by crack propagation at a much lower J (0.818 N/mm) than the material's actual fracture toughness (J_c), which was reported to be 72.8 N/mm [8] under mode I loading conditions at room temperature. A similar analysis is conducted for MCF tests performed by Issa et al. [47] on ultra-fine grained Cr (see Section 4.3), by substituting α = 0.1875, β = 0.575, γ = 4.625. σ_y^t ~2130 MPa for ultra-fine grained Cr and $\bar{P}_{tr}$=1.8 from Fig. 11(a). Further, they recorded an expected P_f ~2.26 mN. From Eq. (5), the w_{min} for valid MCF tests on this material is ~11.37 μm. However, since they performed tests on an MCB specimen with w ~8 μm, the specimen undergoes failure due to plastic collapse, as was discussed in Section 4.3.

From the preceding discussions, it is evident that to determine $\bar{P}_{tr}$ and determine whether the failure is governed by plastic collapse or fracture via crack propagation, a FE simulation of the MCF test, incorporating the correct constitutive response of the tested material needs to be performed. However, it is worth asking if it is possible to ascertain the validity of a fracture test solely from the experimental $\bar{P}-\bar{\delta}$ data with the same degree of confidence. This question can be addressed by reviewing the simulated $\bar{P}-\bar{\delta}$ responses of materials that exhibit different constitutive responses. For materials that exhibit elastic-perfectly plastic constitutive response, such as BMGs, ultra-fine grained and NC alloys (see Figs. 1 and 3(b)), the $\bar{P}-\bar{\delta}$ response is initially linear but becomes non-linear when significant plastic deformation occurs at the crack tip. The slope of the non-linear part of the $\bar{P}-\bar{\delta}$ curves decreases continuously and eventually becomes 0. Irrespective of the material model and specimen dimensions considered, the transition in the failure regime from crack propagation induced fracture to plastic collapse, which is represented by $\bar{P}_{tr}$, occurs the moment $\frac{d\bar{P}}{d\bar{\delta}} \to 0$. Based on this observation, the MCF test of elastic-perfectly plastic materials can be considered invalid if $\frac{d\bar{P}}{d\bar{\delta}}$ ~0 at failure, in the experimentally determined $\bar{P}-\bar{\delta}$ curves. If the test is deemed invalid, a reference value of $\bar{P}_{tr} < \bar{P}_f$ can be chosen from the experimental $\bar{P}-\bar{\delta}$ curves and substituted in Eq. (5), to calculate the appropriate dimensions of MCB specimen that would result in valid MCF tests.

However, in materials that exhibit significant strain hardening the transition in the failure regime may occur much before $\frac{d\bar{P}}{d\bar{\delta}}$ of the $\bar{P}-\bar{\delta}$ curve ~0 (see Fig. 3(b)). This implies that the $\frac{d\bar{P}}{d\bar{\delta}} \rightarrow 0$ cannot be used as a metric to determine the validity of fracture tests in these materials. Therefore, for MCF tests performed on materials that undergo significant strain hardening, complementary FE simulations are necessary for identifying $\bar{P}_{tr}$ and gauging the validity of the test.

4.5. Crack tip constraint effects in MCF specimens

Since the MCF specimen is a relatively new geometry in the fracture mechanics community as compared to the other more studied fracture specimen geometries such as Compact Tension (CT), Single Edge Notched Tension (SENT), Center Cracked Panel (CCP), Single Edge Notched Bend (SENB) and Four Point Bend (4PB) specimens, it is instructive to investigate the local crack tip fields and crack tip constraint in the MCF specimen. Here, we have done this under both 2D plane strain and three dimensions (3D) as the transition in the deformation of the specimen occurs from SSY to LSY. For this purpose, we performed an additional FE simulation of loading of a MCF specimen in 3D. This 3D model has geometry and dimensions identical to the MCF specimen used in the work of Sorensen et al. [9]. The FE mesh and boundary conditions are shown in Fig. S6. It should be noted that in this 3D simulation, instead of the regular rectangular cross-section beam, a realistic pentagonal cross-section beam was used as in the experiments of Sorensen et al. [9]. The cantilever support end of the beam was connected to a large cubic portion of the wall representing the bulk material from which the beam was machined. These cantilever support conditions are very realistic and representative of the actual scenario. In order to facilitate a direct comparison of the crack tip fields in the specimen with the standard HRR fields, we employed von Mises plasticity with Ramberg-Osgood hardening parameter $n = 10$ in the simulation.

We extracted the stress fields ahead of the notch tip from 2D plane strain and 3D FE simulations of loading of the MCF specimens. In the case of 3D, the stress fields at the mid-plane and free side-surface of the specimen were extracted. The variations of normalized hydrostatic stress (σ_h/σ_o) with normalized radial distance ($r/(J/\sigma_o)$) ahead of the notch tip are presented in Fig. 13 (a)–(c) corresponding to 2D plane strain, 3D mid-plane, and 3D free side-surface, respectively. Here, σ_o is the initial yield strength. In each of the subfigures, the stress field obtained from the standard HRR field [62] is presented and compared with those prevailing in the MCF specimen in three different regimes of loading: crack propagation regime (chosen to be the stage where SSY applies), transition point (where LSY applies) and plastic collapse regime (advanced stages of LSY). It can be observed from these figures that the hydrostatic stress prevailing in the MCF specimens ahead of the notch tip is considerably lower than the standard HRR field suggesting a loss of crack tip constraint in the specimen. Furthermore, it can be observed that the hydrostatic stress field decreases progressively as the loading on the specimen increases from the crack propagation regime (SSY), to the transition point (LSY) and to the plastic collapse regime (advanced LSY). Thus, the specimen progressively loses crack tip constraint with loading or deformation.

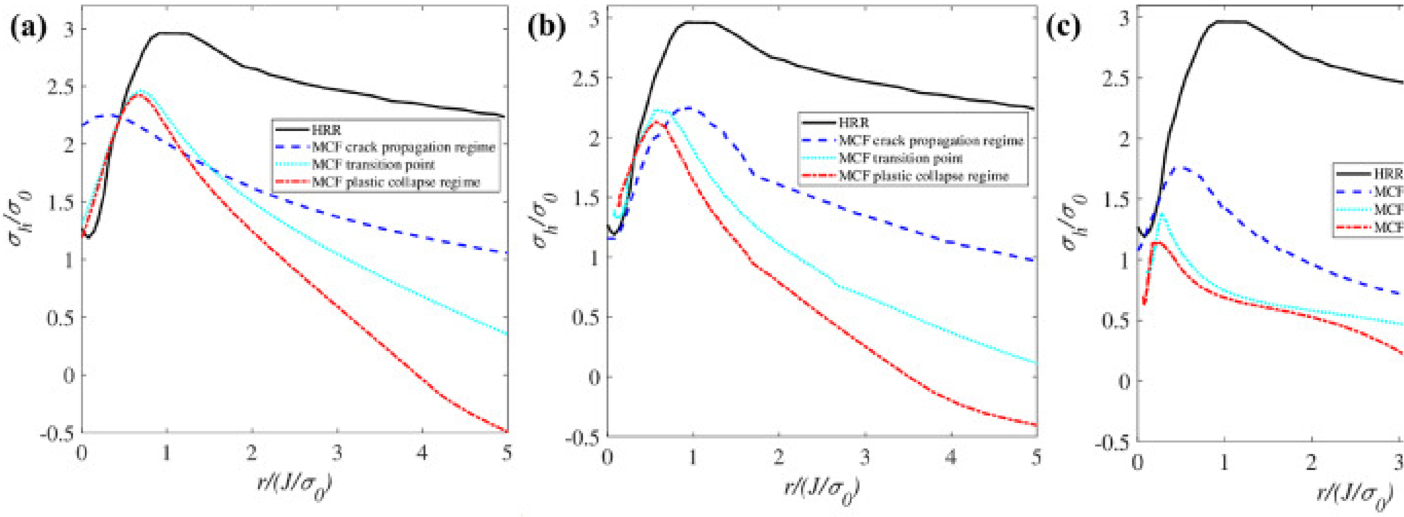

1. Download: Download high-res image (422KB)
2. Download: Download full-size image

Fig. 13. Variations of normalized hydrostatic stress versus normalized radial distance ahead of the notch tip for (a) 2D plane strain, (b) 3D mid-plane, and (c) 3D free side-surface, in the MCF specimens.

In order to quantify the above loss in crack tip constraint, a constraint parameter (Q) is evaluated. Q was first introduced by O'Dowd and Shih [43,62,63] as a part of two parameter (J and Q) description of the elastoplastic crack tip fields called as the J-Q theory. The crack tip fields deep inside the plastic zone are represented by a sum of the HRR fields and a difference field. This difference field corresponds approximately to a uniform hydrostatic shift of the stress field in front of the crack tip. The parameter Q indicates the amplitude of this approximate difference field. The Q parameter is evaluated using the following formula [63]:

(6) $Q=\frac{\sigma_h-(\sigma_h)_{HRR}}{\sigma_0}$ at $\theta=0^o$ and $\frac{r}{\frac{J}{\sigma_0}}=2$

Negative (positive) Q values mean that the hydrostatic stress is reduced (increased) by $Q\sigma_0$ from the Q = 0 reference state. Negative values of Q indicate a loss in crack tip constraint. Table 1 presents the evaluated Q values for 2D plane strain, 3D mid-plane and 3D free side-surface of the MCF specimens at various stages of loading.

Table 1. Constraint (Q) parameter for 2D plane strain, 3D mid-plane, and 3D free side-surface of the MCF specimens at various stages of loading.

Stage of loading	***Q* for 2D plane strain**	***Q* for 3D mid-plane**	***Q* for 3D free side-surface**
MCF crack propagation regime (SSY)	-1.03	-1.05	-1.70
MCF transition point (LSY)	-1.15	-1.54	-2.08

Stage of loading	Q for 2D plane strain	Q for 3D mid-plane	Q for 3D free side-surface
MCF plastic collapse regime (advanced LSY)	-1.40	-1.86	-2.14

It can be noted from Table 1 that there is a considerable constraint loss (Q = -1.03) in the MCF specimen even in the crack propagation (SSY) regime under 2D plane strain. In the same regime, for the 3D MCF specimen, there is a similar constraint loss (Q = -1.05) at the mid-plane but substantially higher constraint loss (Q = -1.70) at the free side-surface which is understandable as it is a traction free surface. With progressive increase in loading, as the deformation transitions from SSY to LSY, to advanced LSY, Q becomes increasingly negative (see Table 1). Thus, the highest constraint loss is in the plastic collapse or advanced LSY regime.

The normalized P-δ and J-P curves corresponding to the 3D MCF specimen simulation are displayed in Fig. 14. The points corresponding to the three stages of loading, mentioned in Table 1, namely: MCF crack propagation regime (SSY), MCF transition point (LSY), and MCF plastic collapse regime (advanced LSY) are indicated on the curves. Similarly, the corresponding points for the 2D plane strain case mentioned in Table 1 are indicated on normalized P-δ and J-P curves for n = 10 in Fig. 3(b) and (c) by hollow square, star and filled square symbols, respectively.

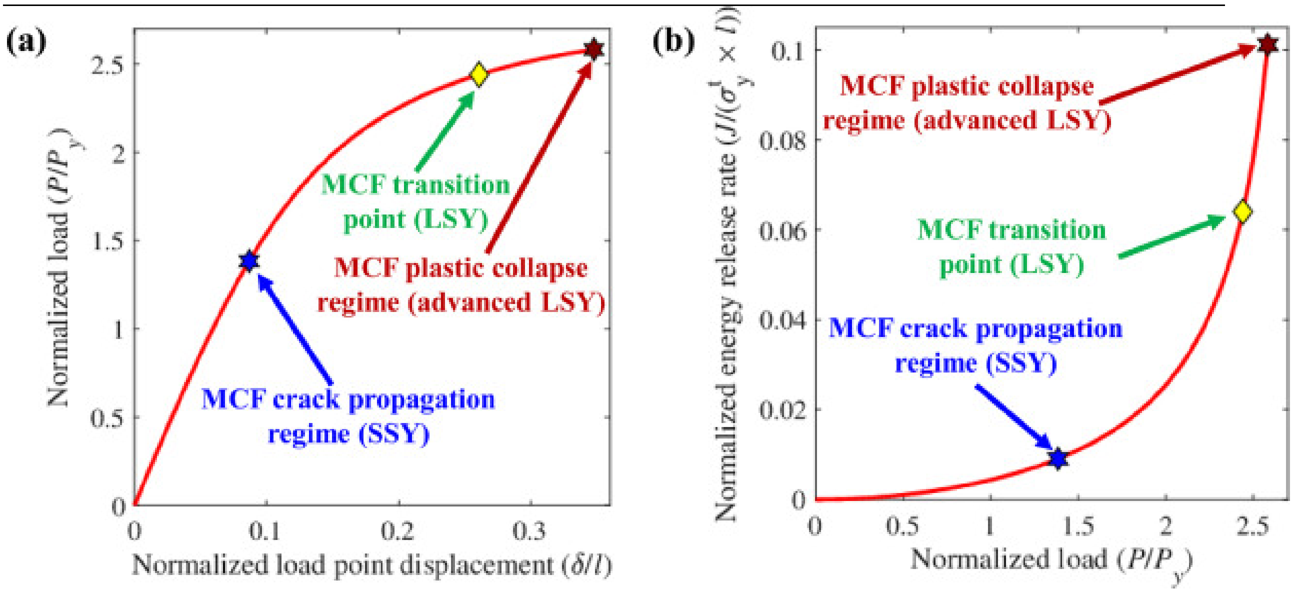

1. Download: Download high-res image (524KB)
2. Download: Download full-size image

Fig. 14. (a) Normalized P versus δ, and (b) normalized J versus P curves for the 3D MCF specimen simulation. The points corresponding to the three stages of loading mentioned in Table 1 are indicated on the curves.

Contour plots of PEEQ in the 3D MCF specimen at crack propagation regime (SSY), at transition point (LSY), and at the plastic collapse regime (advanced LSY) are displayed in Fig. S7. It can be observed from this figure that, initially, the notch tip region, top and bottom of the beam undergo plastic deformation. Further loading results in linking of the plastic zone at the top of the beam with that near the notch tip. This combined plastic zone later interacts with the plastic zone present at the bottom of beam causing a plastic hinge to form and the MCF specimen to fail due to plastic collapse.

The implications of the above results are discussed next. The crack tip constraint in the 3D MCF specimen at the free side-surface is lower than that at the mid-plane which means that the crack is more likely to initiate form the mid plane rather than at the free side-surface. The near tip fields ahead of the notch tip in the MCF specimen are not reaching the HRR level of triaxiality due to constraint loss. One of the reasons of this constraint loss could be the lower value of a/w = 0.3 considered in this work. It could also be an intrinsic characteristic of the MCF specimen as is the case for CCP and SENB specimens [43]. A consequence of the loss in crack tip constraint in the MCF specimen is that the activation of stress-controlled fracture micro-mechanisms might get delayed or suppressed altogether due to hydrostatic stress levels ahead of the crack tip not reaching critical values [64] required for fracture initiation. If crack initiation gets delayed or suppressed in the MCF specimen due to loss in constraint, the specimen is more likely to fail due to plastic collapse invalidating the fracture test.

5. Summary and conclusions

In this paper, a normalization scheme is proposed which results in load versus load-point-displacement curves, and energy release rate versus load curves of micro- and bulk CB fracture specimens to fall on master curves. The effects of CB fracture specimen aspect ratios, material hardening, and YC parameters on the master curves is investigated. While t/w is found to have no effect on the master curves, different values of a/w, l/w, n and μ result in a family of master curves. A transition point divides the master curves into two regimes which correspond to failure of the specimen by crack propagation, and that by plastic collapse of the uncracked ligament. The transition point on the master curves corresponds to the stage of loading of the specimen when the plastic zone around the notch tip starts interacting with the plastic zone at the bottom of the CB specimen. Beyond the transition point, the entire crack ligament undergoes plastic deformation, forms a plastic hinge causing specimen rotation followed by its failure by plastic collapse.

The implications of present results on the validity of MCF tests, interpretation of their failure regimes and size effects on fracture toughness are discussed. An expression is derived for the minimum size requirement of the MCF specimen in order to get valid fracture tests.

Application of the proposed failure regimes of MCF specimens to isotropic, elastoplastic materials such BMGs, NC materials and UFG materials are discussed. While the failure points of bulk specimens made of BMGs and UFG materials lie in the regime of fracture due to crack propagation, failure points of some MCF specimens of these materials taken from literature lie in the regime of failure due to plastic collapse, suggesting invalid fracture tests and possibly incorrect interpretation of size effects. However, it is found that failure points of all the fracture specimens made of NC materials considered from literature fall in the regime of failure due to crack propagation implying valid fracture tests.

Before closing, it must be mentioned that the present results have important implications for the design of MCB fracture specimens, interpretation of their failure regimes, assessment of validity of test data, and potential size-effects on fracture toughness, as measured through the micro-cantilever beam fracture test which has become a popular technique in recent times for micro-scale fracture toughness measurement of several technologically important materials. Lastly, it should be highlighted that although the present results are discussed in the context of micro-cantilever fracture specimens, the analyses performed, and results discussed here are valid not only for micro-cantilever fracture specimens but also hold for all sizes (nano/micro/milli/macro-sized) of notched cantilever beam fracture specimens. This is due to the proposed normalization scheme for $\bar{P}-\bar{\delta}$ and $\bar{J}-\bar{P}$ curves and the fact that the constitutive models used in the present simulations do not incorporate any material length scale.

Declaration of Competing Interest

The authors declare that they have no known competing financial interests or personal relationships that could have appeared to influence the work reported in this paper.

Acknowledgments

DR's visit to NTU, where some of the simulations reported in this work were performed, was supported by an IITB-NTU joint Ph.D. Degree Program. Rest of the simulations were performed at IIT Bombay, for which DR would like to acknowledge the financial support via a Teaching Assistantship received for doctoral studies at IIT Bombay from MHRD, Government of India. RLN acknowledges funding and support from the Start-up Research grant (SRG/2020/000095) of the Science and Engineering Research Board, DST, GoI. Research at NTU was supported by the Structural Metal Alloys Program (Grant Ref. No. A18b1B0061) of the Agency for Science, Technology and Research of Singapore.

Appendix. Supplementary materials

Download: Download Acrobat PDF file (1MB)

References

[1]

C.A. Schuh, T.C. Hufnagel, U. Ramamurty

Mechanical behavior of amorphous alloys

Acta Mater., 55 (2007), pp. 4067-4109, 10.1016/j.actamat.2007.01.052
View PDFView articleView in ScopusGoogle Scholar
[2]

A. Bhattacharyya, G. Singh, K. Eswar Prasad, R. Narasimhan, U. Ramamurty

On the strain rate sensitivity of plastic flow in metallic glasses

Mater. Sci. Eng. A, 625 (2015), pp. 245-251, 10.1016/j.msea.2014.12.004
View PDFView articleView in ScopusGoogle Scholar
[3]

O.V Kuzmin, Y.T. Pei, C.Q. Chen, J.T.M. De Hosson

Intrinsic and extrinsic size effects in the deformation of metallic glass nanopillars

Acta Mater, 60 (2012), pp. 889-898, 10.1016/j.actamat.2011.11.023
View PDFView articleView in ScopusGoogle Scholar
[4]

V. Hasannaeimi, S. Muskeri, B. Gwalani, D.C. Hofmann, S. Mukherjee

Deformation behavior of metallic glass composites and plasticity accommodation at microstructural length-scales

Mater. Today Commun., 24 (2020), Article 101237, 10.1016/j.mtcomm.2020.101237
View PDFView articleView in ScopusGoogle Scholar
[5]

J. Ast, M. Ghidelli, K. Durst, M. Göken, M. Sebastiani, A.M. Korsunsky

A review of experimental approaches to fracture toughness evaluation at the micro-scale

Mater. Des., 173 (2019), Article 107762, 10.1016/j.matdes.2019.107762
View PDFView articleView in ScopusGoogle Scholar

[6]

N. Warthi, P. Ghosh, A.H. Chokshi

Approaching theoretical strengths by synergistic internal and external size refinement

Scr. Mater., 68 (2013), pp. 225-228, 10.1016/j.scriptamat.2012.09.029
View PDFView articleView in ScopusGoogle Scholar
[7]

R.L. Narayan, K. Boopathy, I. Sen, D.C. Hofmann, U. Ramamurty

On the hardness and elastic modulus of bulk metallic glass matrix composites

Scr. Mater., 63 (2010), pp. 768-771, 10.1016/j.scriptamat.2010.06.010
View PDFView articleView in ScopusGoogle Scholar
[8]

D. Raut, R.L. Narayan, P. Tandaiya, U. Ramamurty

Temperature-dependence of mode I fracture toughness of a bulk metallic glass

Acta Mater., 144 (2018), pp. 325-336, 10.1016/j.actamat.2017.10.063
View PDFView articleView in ScopusGoogle Scholar
[9]

D. Sorensen, E. Hintsala, J. Stevick, J. Pischlar, B. Li, D. Kiener, J.C. Myers, H. Jin, J. Liu, D. Stauffer, A.J. Ramirez, R.O. Ritchie

Intrinsic toughness of the bulk-metallic glass Vitreloy 105 measured using micro-cantilever beams

Acta Mater., 183 (2020), pp. 242-248, 10.1016/j.actamat.2019.11.021
View PDFView articleView in ScopusGoogle Scholar
[10]

D. Jang, J.R. Greer

Transition from a strong-yet-brittle to a stronger-and-ductile state by size reduction of metallic glasses

Nat. Mater., 9 (2010), pp. 215-219, 10.1038/nmat2622
View in ScopusGoogle Scholar
[11]

D. Jang, C.T. Gross, J.R. Greer

Effects of size on the strength and deformation mechanism in Zr-based metallic glasses

Int. J. Plast., 27 (2011), pp. 858-867, 10.1016/j.ijplas.2010.09.010
View PDFView articleView in ScopusGoogle Scholar
[12]

J.R. Greer, J.T.M. De Hosson

Plasticity in small-sized metallic systems: intrinsic versus extrinsic size effect

Prog. Mater. Sci., 56 (2011), pp. 654-724, 10.1016/j.pmatsci.2011.01.005
View PDFView articleView in ScopusGoogle Scholar
[13]

C.Q. Chen, Y.T. Pei, J.T.M. De Hosson

Effects of size on the mechanical response of metallic glasses investigated through *in situ* TEM bending and compression experiments
Acta Mater., 58 (2010), pp. 189-200, 10.1016/j.actamat.2009.08.070
View PDFView articleView in ScopusGoogle Scholar
[14]

A. Bharathula, S.W. Lee, W.J. Wright, K.M. Flores

Compression testing of metallic glass at small length scales: effects on deformation mode and stability

Acta Mater, 58 (2010), pp. 5789-5796, 10.1016/j.actamat.2010.06.054
View PDFView articleView in ScopusGoogle Scholar
[15]

C.J. Lee, J.C. Huang, T.G. Nieh

Sample size effect and microcompression of Mg65Cu25Gd10 metallic glass

Appl. Phys. Lett., 91 (2007), Article 161913, 10.1063/1.2800313
View in ScopusGoogle Scholar
[16]

A.S. Khan, S. Huang

Continuum Theory of Plasticity

Wiley (1995)

https://books.google.co.in/books?id=I1FPaaY355gC
Google Scholar
[17]

R. Walter, W.R. Osgood

Description of stress-strain curves by three parameters

Natl. Advis. Comm. Aeronaut. (1943), pp. 1-29

http://www.apesolutions.com/spd/public/NACA-TN902.pdf
CrossrefGoogle Scholar
[18]

L. Anand, C. Su

A theory for amorphous viscoplastic materials undergoing finite deformations, with application to metallic glasses

J. Mech. Phys. Solids, 53 (2005), pp. 1362-1396, 10.1016/j.jmps.2004.12.006
View PDFView articleView in ScopusGoogle Scholar
[19]

R. Bhowmick, R. Raghavan, K. Chattopadhyay, U. Ramamurty

Plastic flow softening in a bulk metallic glass

Acta Mater., 54 (2006), pp. 4221-4228, 10.1016/j.actamat.2006.05.011
View PDFView articleView in ScopusGoogle Scholar
[20]

P.E. Donovan

A yield criterion for Pd40Ni40P20 metallic glass

Acta Metall., 37 (1989), pp. 445-456, 10.1016/0001-6160(89)90228-9
View PDFView articleView in ScopusGoogle Scholar
[21]

J.J. Lewandowski, P. Lowhaphandu

Effects of hydrostatic pressure on the flow and fracture of a bulk amorphous metal

Philos. Mag. A, 82 (2002), pp. 3427-3441, 10.1080/01418610208240453
View in ScopusGoogle Scholar
[22]

R. Vaidyanathan, M. Dao, G. Ravichandran, S. Suresh

Study of mechanical deformation in bulk metallic glass through instrumented indentation

Acta Mater., 49 (2001), pp. 3781-3789, 10.1016/S1359-6454(01)00263-4
View PDFView articleView in ScopusGoogle Scholar
[23]

C.A. Schuh, A.C. Lund

Atomistic basis for the plastic yield criterion of metallic glass

Nat. Mater., 2 (2003), p. 449, 10.1038/nmat918
–
View in ScopusGoogle Scholar
[24]

P. Tandaiya, U. Ramamurty, R. Narasimhan

On numerical implementation of an isotropic elastic–viscoplastic constitutive model for bulk metallic glasses

Model. Simul. Mater. Sci. Eng., 19 (2010), p. 15002, 10.1088/0965-0393/19/1/015002
Google Scholar
[25]

S. Gouripriya, P. Tandaiya

Mechanisms of compressive deformation and failure of porous bulk metallic glasses

Model. Simul. Mater. Sci. Eng., 25 (2017), p. 45006, 10.1088/1361-651x/aa67b0
Google Scholar
[26]

S. Gouripriya, P. Tandaiya

Mechanistic origins of work hardening in shape memory alloy particle reinforced *ex-situ* bulk metallic glass matrix composites
Scr. Mater., 185 (2020), pp. 1-6, 10.1016/j.scriptamat.2020.04.013

View PDFView articleView in ScopusGoogle Scholar
[27]

S. Gouripriya, P. Tandaiya

Three-dimensional unit cell study of a porous bulk metallic glass under various stress states

J. Appl. Mech., 86 (2019), p. 61010, 10.1115/1.4042995
Google Scholar
[28]

P. Tandaiya, U. Ramamurty, G. Ravichandran, R. Narasimhan

Effect of poisson's ratio on crack tip fields and fracture behavior of metallic glasses

Acta Mater., 56 (2008), pp. 6077-6086, 10.1016/j.actamat.2008.08.018
View PDFView articleView in ScopusGoogle Scholar
[29]

P. Tandaiya, U. Ramamurty, R. Narasimhan

Mixed mode (I and II) crack tip fields in bulk metallic glasses

J. Mech. Phys. Solids, 57 (2009), pp. 1880-1897, 10.1016/j.jmps.2009.07.006
View PDFView articleView in ScopusGoogle Scholar
[30]

P. Tandaiya, R. Narasimhan, U. Ramamurty

On the mechanism and the length scales involved in the ductile fracture of a bulk metallic glass

Acta Mater., 61 (2013), pp. 1558-1570, 10.1016/j.actamat.2012.11.033
View PDFView articleView in ScopusGoogle Scholar
[31]

P. Tandaiya, R. Narasimhan, U. Ramamurty

Mode I crack tip fields in amorphous materials with application to metallic glasses

Acta Mater., 55 (2007), pp. 6541-6552, 10.1016/j.actamat.2007.08.017
View PDFView articleView in ScopusGoogle Scholar
[32]

S. Gouripriya, P. Tandaiya

Mechanistic origins of work hardening in shape memory alloy particle reinforced *ex-situ* bulk metallic glass matrix composites
Scr. Mater., 185 (2020), pp. 1-6, 10.1016/j.scriptamat.2020.04.013
View PDFView articleView in ScopusGoogle Scholar
[33]

V. Keryvin, K. Eswar Prasad, Y. Gueguen, J.C. Sanglebœuf, U. Ramamurty

Temperature dependence of mechanical properties and pressure sensitivity in metallic glasses below glass transition

Philos. Mag., 88 (2008), pp. 1773-1790, 10.1080/14786430802286971
View in ScopusGoogle Scholar
[34]

J. Lu, G. Ravichandran

Pressure-dependent flow behavior of $Zr_{41.2}Ti_{13.8}Cu_{12.5}Ni10Be_{22.5}$ bulk metallic glass
J. Mater. Res., 18 (2003), pp. 2039-2049, 10.1557/JMR.2003.0287
View in ScopusGoogle Scholar
[35]

M.N.M. Patnaik, R. Narasimhan, U. Ramamurty

Spherical indentation response of metallic glasses

Acta Mater., 52 (2004), pp. 3335-3345, 10.1016/j.actamat.2004.03.028
View PDFView articleGoogle Scholar
[36]

U. Ramamurty, S. Jana, Y. Kawamura, K. Chattopadhyay

Hardness and plastic deformation in a bulk metallic glass

Acta Mater., 53 (2005), pp. 705-717, 10.1016/j.actamat.2004.10.023
View PDFView articleView in ScopusGoogle Scholar
[37]

P. Kontis, M. Köhler, S. Evertz, Y.T. Chen, V. Schnabel, R. Soler, J. Bednarick, C. Kirchlechner, G. Dehm, D. Raabe, J.M. Schneider, B. Gault

Nano-laminated thin film metallic glass design for outstanding mechanical properties

Scr. Mater., 155 (2018), pp. 73-77, 10.1016/j.scriptamat.2018.06.015
View PDFView articleView in ScopusGoogle Scholar
[38]

C.L. Li, J.P. Chu, J.W. Lee

Measuring notch toughness of thin film metallic glasses using focused ion beam-based microcantilever method: comparison with Ti and TiN crystalline films

Mater. Sci. Eng. A, 698 (2017), pp. 104-109, 10.1016/j.msea.2017.05.002
View PDFView articleView in ScopusGoogle Scholar
[39]

V. Schnabel, B.N. Jaya, M. Köhler, D. Music, C. Kirchlechner, G. Dehm, D . Raabe, J.M. Schneider

Electronic hybridisation implications for the damage-tolerance of thin film metallic glasses

Sci. Rep., 6 (2016), p. 36556, 10.1038/srep36556
View in ScopusGoogle Scholar
[40]

Y. Chen, X. Zhang, C.J. Williams, G. Brewster, P. Xiao

Determination of fracture toughness of a platinum-modified nickel aluminide coating by micromechanical testing

Materialia, 20 (2021), Article 101267, 10.1016/j.mtla.2021.101267
View PDFView articleView in ScopusGoogle Scholar
[41]

E.P. Popov

Engineering Mechanics of Solids

(2nd ed), Prentice-Hall Of India Pvt. Limited (1998)

https://books.google.co.in/books?id=UkBNPgAACAAJ
Google Scholar
[42]

A.A. Griffith, G.I. Taylor

The phenomena of rupture and flow in solids

Philos. Trans. R. Soc. Lond. Ser. A Contain. Pap. Math. Phys. Character, 221 (1921), pp. 163-198, 10.1098/rsta.1921.0006
View in ScopusGoogle Scholar
[43]

N. O'Dowd, C. Shih

Family of crack-tip fields characterized by triaxiality parameter-I. Structure of fields

J. Mech. Phys. Solids (1991), p. 39

Google Scholar
[44]

D.L. Crane, T.L. Anderson

Deformation Limits on Two-Parameter Fracture Mechanics in Terms of Higher Order Asymptotics

(Texas A&M University, College Station) (1994)

AAAB(Texas A&M University, College Station)

https://ui.adsabs.harvard.edu/abs/1994tamu.reptS....C
Google Scholar
[45]

T.L. Anderson

Fracture Mechanics Fundamentals and Applications, 688, Taylor & Francis Group (2017), 10.1201/9781315370293
Google Scholar
[46]

S. Evertz, I. Kirchlechner, R. Soler, C. Kirchlechner, P. Kontis, J. Bednarci k, B. Gault, G. Dehm, D. Raabe, J.M. Schneider

Electronic structure based design of thin film metallic glasses with superior fracture toughness

Mater. Des., 186 (2020), Article 108327, 10.1016/j.matdes.2019.108327
View PDFView articleView in ScopusGoogle Scholar
[47]

I. Issa, A. Hohenwarter, R. Fritz, D. Kiener

Fracture properties of ultrafine grain chromium correlated to single dislocation processes at room temperature

J. Mater. Res., 34 (2019), pp. 2370-2383, 10.1557/jmr.2019.140
View in ScopusGoogle Scholar
[48]

R. Qu, R. Maaß, Z. Liu, D. Tönnies, L. Tian, R.O. Ritchie, Z. Zhang, C.A. Volkert

Flaw-insensitive fracture of a micrometer-sized brittle metallic glass

Acta Mater., 218 (2021), Article 117219, 10.1016/j.actamat.2021.117219
View PDFView articleView in ScopusGoogle Scholar
[49]

A.C. Lund, C.A. Schuh

The Mohr-Coulomb criterion from unit shear processes in metallic glass

Intermetallics, 12 (2004), pp. 1159-1165, 10.1016/j.intermet.2004.07.001
View PDFView articleView in ScopusGoogle Scholar
[50]

A.C. Lund, C.A. Schuh

Yield surface of a simulated metallic glass

Acta Mater., 51 (2003), pp. 5399-5411, 10.1016/S1359-6454(03)00396-3
View PDFView articleView in ScopusGoogle Scholar
[51]

W. Chen, Z. Liu, J. Ketkaew, R.M.O. Mota, S.H. Kim, M. Power, W. Samela, J. Schroers

Flaw tolerance of metallic glasses

Acta Mater., 107 (2016), pp. 220-228, 10.1016/j.actamat.2016.02.002
View PDFView articleView in ScopusGoogle Scholar
[52]

R.L. Narayan, D. Raut, U. Ramamurty

A quantitative connection between shear band mediated plasticity and fracture initiation toughness of metallic glasses

Acta Mater., 150 (2018), pp. 69-77, 10.1016/j.actamat.2018.03.011
View PDFView articleView in ScopusGoogle Scholar
[53]

Q. He, Y.Q. Cheng, E. Ma, J. Xu

Locating bulk metallic glasses with high fracture toughness: chemical effects and composition optimization

Acta Mater., 59 (2011), pp. 202-215, 10.1016/j.actamat.2010.09.025
View PDFView articleView in ScopusGoogle Scholar
[54]

M.G. Mueller, V. Pejchal, G. Žagar, A. Singh, M. Cantoni, A. Mortensen

Fracture toughness testing of nanocrystalline alumina and fused quartz using chevron-notched microbeams

Acta Mater., 86 (2015), pp. 385-395, 10.1016/j.actamat.2014.12.016
View PDFView articleView in ScopusGoogle Scholar
[55]

Y. Xiao, Y. Zou, H. Ma, A.S. Sologubenko, X. Maeder, R. Spolenak, J.M. Wheeler

Nanostructured NbMoTaW high entropy alloy thin films: high strength and enhanced fracture toughness

Scr. Mater., 168 (2019), pp. 51-55, 10.1016/j.scriptamat.2019.04.011
View PDFView articleGoogle Scholar
[56]

R. Henry, T. Blay, T. Douillard, A. Descamps-Mandine, I. Zacharie-Aubrun, J.M. Gatt, C. Langlois, S. Meille

Local fracture toughness measurements in polycrystalline cubic zirconia using micro-cantilever bending tests

Mech. Mater., 136 (2019), Article 103086, 10.1016/j.mechmat.2019.103086
View PDFView articleView in ScopusGoogle Scholar
[57]

K. Yoshida, F. Wakai, N. Nishiyama, R. Sekine, Y. Shinoda, T. Akatsu, T. Nagoshi, M. Sone

Large increase in fracture resistance of stishovite with crack extension less than one micrometer

Sci. Rep., 5 (2015), p. 10993, 10.1038/srep10993
Google Scholar
[58]

W. Cao, C. Marvel, D. Yin, Y. Zhang, P. Cantwell, M.P. Harmer, J. Luo, R. P. Vinci

Correlations between microstructure, fracture morphology, and fracture toughness of nanocrystalline Ni–W alloys

Scr. Mater., 113 (2016), pp. 84-88, 10.1016/j.scriptamat.2015.09.030
View PDFView articleView in ScopusGoogle Scholar
[59]

M.A. Morris-Muñoz, A. Dodge, D.G. Morris

Structure, strength and toughness of nanocrystalline FeAl

Nanostruct. Mater., 11 (1999), pp. 873-885, 10.1016/S0965-9773(99)00385-2
View PDFView articleView in ScopusGoogle Scholar
[60]

A.K. Saxena, S. Brinckmann, B. Völker, G. Dehm, C. Kirchlechner

Experimental conditions affecting the measured fracture toughness at the microscale: notch geometry and crack extension measurement

Mater. Des., 191 (2020), Article 108582, 10.1016/j.matdes.2020.108582
View PDFView articleView in ScopusGoogle Scholar
[61]

J. Ast, M. Göken, K. Durst

Size-dependent fracture toughness of tungsten

Acta Mater., 138 (2017), pp. 198-211, 10.1016/j.actamat.2017.07.030
View PDFView articleView in ScopusGoogle Scholar
[62]

N.P. O'Dowd, C.F. Shih

Family of crack-tip fields characterized by a triaxiality parameter—II. Fracture applications

J. Mech. Phys. Solids, 40 (1992), pp. 939-963, 10.1016/0022-5096(92)90057-9
View PDFView articleView in ScopusGoogle Scholar
[63]

N.P. O'dowd

Applications of two parameter approaches in elastic-plastic fracture mechanics

Eng. Fract. Mech., 52 (1995), pp. 445-465, 10.1016/0013-7944(95)00033-R
View PDFView articleView in ScopusGoogle Scholar
[64]

R.O. Ritchie, J.F. Knott, J.R. Rice

On the relationship between critical tensile stress and fracture toughness in mild steel

J. Mech. Phys. Solids, 21 (1973), pp. 395-410, 10.1016/0022-5096(73)90008-2
View PDFView articleView in ScopusGoogle Scholar
[65]

D. Sorensen, E. Hintsala, J. Stevick, J. Pischlar, B. Li, D. Kiener, J.C. Myers, H. Jin, J. Liu, D. Stauffer, A.J. Ramirez, R.O. Ritchie

Intrinsic toughness of the bulk-metallic glass Vitreloy 105 measured using micro-cantilever beams

Acta Mater., 183 (2020), pp. 242-248

(with permission from Elsevier) Reprinted from

View PDFView articleView in ScopusGoogle Scholar
[66]

R. Qu, R. Maaß, Z. Liu, D. Tönnies, L. Tian, R.O. Ritchie, Z. Zhang, C.A. Volkert

Flaw-insensitive fracture of a micrometer-sized brittle metallic glass

Acta Mater., 218 (2021), Article 117219

(with permission from Elsevier), Reprinted from

View PDFView articleView in ScopusGoogle Scholar
[67]

Y. Xiao, Y. Zou, H. Ma, A.S. Sologubenko, X. Maeder, R. Spolenak, J.M. Wheeler

Nanostructured NbMoTaW high entropy alloy thin films: high strength and enhanced fracture toughness

Scr. Mater., 168 (2019), pp. 51-55

(with permission from Elsevier) Reprinted from

View PDFView articleGoogle Scholar
[68]

J. Ast, M. Göken, K. Durst

Size-dependent fracture toughness of tungsten

Acta Mater., 138 (2017), pp. 198-211

(with permission from Elsevier) Reprinted from

View PDFView articleView in ScopusGoogle Scholar